Inorganic Chemistry

Article

Cite This: *Inorg. Chem.* 2019, 58, 12334−12347

pubs.acs.org/IC

Organoruthenated Nitroxoline Derivatives Impair Tumor Cell Invasion through Inhibition of Cathepsin B Activity

Ana Mitrović,[†,‡,∥] Jakob Kljun,[§,∥] Izidor Sosič,[†] Matija Uršič,[§] Anton Meden,[§] Stanislav Gobec,[†] Janko Kos,[*,†,‡] and Iztok Turel[*,§]

[†]Faculty of Pharmacy, University of Ljubljana, Aškerčeva c. 7, SI-1000 Ljubljana, Slovenia

[‡]Department of Biotechnology, Jožef Stefan Institute, Jamova c. 39, SI-1000 Ljubljana, Slovenia

[§]Faculty of Chemistry and Chemical Technology, University of Ljubljana, Večna pot 113, SI-1000 Ljubljana, Slovenia

Supporting Information

ABSTRACT: Lysosomal cysteine peptidase cathepsin B (catB) is an important tumor-promoting factor involved in tumor progression and metastasis representing a relevant target for the development of new antitumor agents. In the present study, we synthesized 11 ruthenium compounds bearing either the clinical agent nitroxoline that was previously identified as potent selective reversible inhibitor of catB activity or its derivatives. We demonstrated that organoruthenation is a viable strategy for obtaining highly effective and specific inhibitors of catB endo- and exopeptidase activity, as shown using enzyme kinetics and microscale thermophoresis. Furthermore, we showed that the novel metallodrugs by catB inhibition significantly impair processes of tumor progression in in vitro cell based functional assays at low noncytotoxic concentrations. Generally, by using metallodrugs we observed an improvement in catB inhibition, a reduction of extracellular matrix degradation and tumor cell invasion in comparison to free ligands, and a correlation with the reactivity of the monodentate halide leaving ligand.

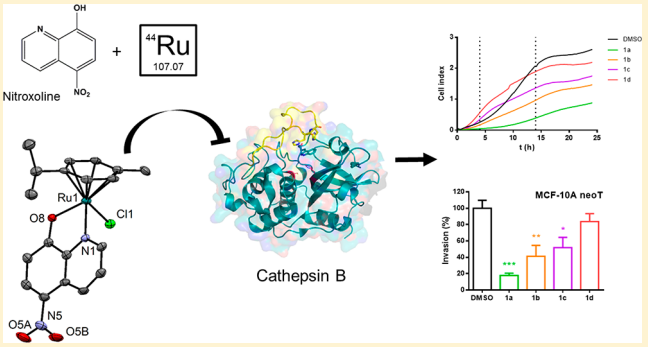

INTRODUCTION

Cathepsin B (EC 3.4.22.1; catB) is a lysosomal cysteine peptidase that belongs to clan CA of the papain family (C1). The proteolytic activity of this enzyme is crucial in the mechanisms of cancer progression. Specifically, it has been identified as an important tumor-promoting factor[1−3] involved in extracellular matrix degradation, a process which enables tumor migration, invasion, metastasis, and angiogenesis.[1−4] CatB is unique in its structure among cysteine cathepsins by possessing an occluding loop, a 20 amino acid insertion, which defines whether the enzyme acts as an endopeptidase or an exopeptidase.[5−9]

At low pH, present within lysosomes, salt bridges hold the occluding loop in the closed conformation, attached on the body of the enzyme, and prevent access of protein substrates to the active site cleft and consequently catB acts as an exopeptidase.[8,9] At higher pH the salt bridges are weakened, resulting in conformational change, which enables the access of protein substrates to the active site and endopeptidase activity of catB.[6,9] The endopeptidase activity of catB, with the optimum at neutral pH, is mainly associated with its pathological role, including processes of cancer progression.[10] However, we have demonstrated previously that, in addition to endopeptidase activity, catB exopeptidase activity also contributes to tumor progression.[11] High pharmacological relevance of catB has been established in various tumor mouse models, validating this enzyme as a target for new chemotherapeutic strategies.[12−14]

In 2011, we identified the antibacterial agent nitroxoline (**nxH**), a member of the 8-hydroxyquinolone (hq) family, as a potent reversible inhibitor of catB (Figure 1; left).[15] Nitroxoline binds to the S2′ subsite of the catB active site cleft, for which active site mapping of catB with substrates and inhibitors revealed a preference for large aromatic residues.[15,16] The crystal structure of the enzyme−inhibitor complex revealed that the interaction of the nitro group of **nxH** with two histidine residues (His110 and His 111) is crucial for binding into an active site, whereas the quinoline ring nitrogen N1 and the hydroxyl group at position 8 are not involved in direct interactions with the protein. Nitroxoline was found to potently impair tumor progression in both in vitro and in vivo models, and these effects correlated with catB inhibition.[17] This discovery was followed by a structure−activity relationship study of over 50 compounds with structural modifications at positions 2, 5, 7, and 8 and within the quinoline ring. In comparison with the parent **nxH**, the 7-aminomethyl-8-hydroxy-5-nitroquinoline derivatives (Figure 1; center top)

Received: June 25, 2019
Published: August 29, 2019

DOI: 10.1021/acs.inorgchem.9b01882
Inorg. Chem. 2019, 58, 12334−12347

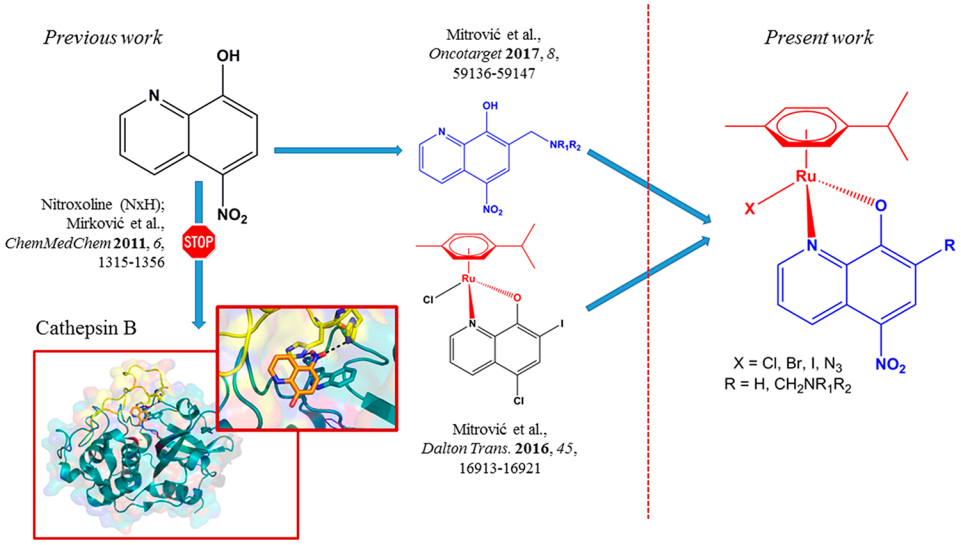

Figure 1. Summary of previous and present work: (left) discovery of nitroxoline (nxH) as a catB inhibitor; (top center) development of selective catB inhibitors based on a SAR study; (center bottom) discovery of an organoruthenium catB inhibitor; (right) organoruthenium-nitroxolinato complexes presented in this work.

Table 1. Structures of Synthesized Organoruthenium Complexes with Nitroxoline and Its Derivatives

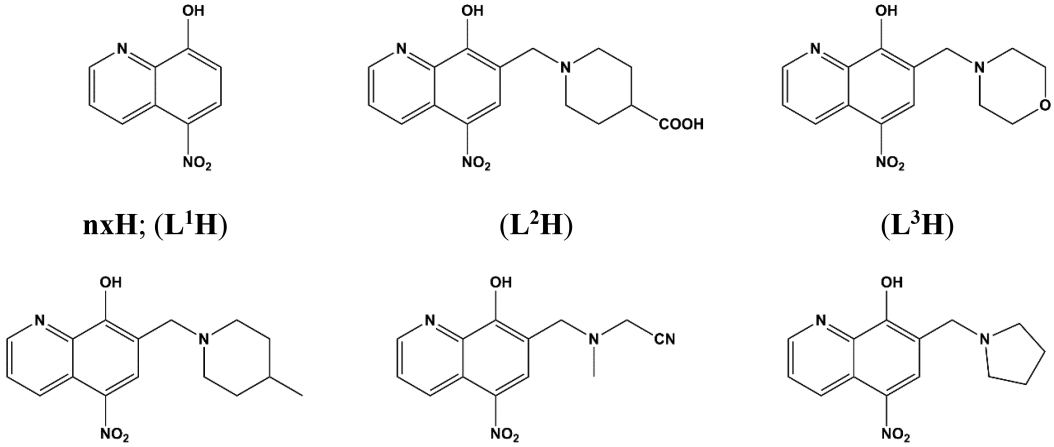

nxH; (L^1H) **(L^2H)** **(L^3H)**

(L^4H) **(L^5H)** **(L^6H)**

Ligand\Complex	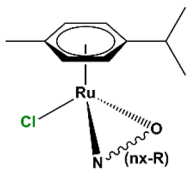	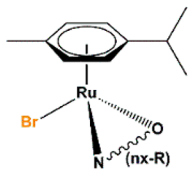	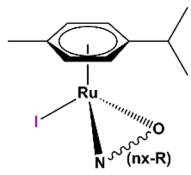	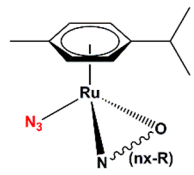
nxH; (L^1H)	**1a**[44]	**1b**	**1c**	**1d**
(L^2H)	**2a**	**2b**		
(L^3H)	**3a**		**3c**	
(L^4H)	**4a**			
(L^5H)	**5a**			
(L^6H)	**6a**			

showed improved endopeptidase activity inhibition and selectivity against other cathepsins.[15,18,19] Moreover, one compound from this class was highly effective in in vitro and in vivo cancer models by regulating catB activity.[20]

Metallodrugs are very important parts of cancer chemotherapeutics as, for example, 7 out of the 10 most commonly used combination therapies include one of three globally used platinum-based agents: cisplatin, oxaliplatin, or carboplatin.[21]

DOI: 10.1021/acs.inorgchem.9b01882
Inorg. Chem. 2019, 58, 12334−12347

Those agents, however, possess serious downfalls as patients often develop resistance to platinum-based agents or display severe side effects. The importance of metals other than platinum is corroborated by the fact that compounds of gallium,[22] copper,[23] titanium,[24] and, most prominently, three ruthenium compounds have entered clinical trials.[25−27] In recent years, we have been intensely investigating the biological properties and anticancer potential of metal complexes of hydroxyquinolines.[28−34] For instance, we synthesized an organoruthenium complex (Figure 1; center bottom) of clioquinol (**cqH**) and showed that the complex (**Ru-cq**) exhibits selective toxicity toward leukemic cell lines through a caspase-dependent mechanism of cell death.[28] Moreover, we determined that the complex **Ru-cq** does not interact with DNA and shows proteasome-independent inhibition of the NFκB signaling pathway without affecting cell-cycle distribution.[28] A more detailed study revealed that the complex is a low micromolar inhibitor of catB and impairs the degradation of extracellular matrix and tumor cell invasion at noncytotoxic concentrations, which revealed a specific anticancer mechanism not related to the general intrinsic toxicity.[29]

Cathepsin B has previously been investigated as a potential target for metalloinhibitors, most notably, compounds of gold,[35] rhenium,[36] and ruthenium.[37−40] Despite intensive investigations no structural data are available for catB metalloinhibitors. It is, however, generally accepted that they act through direct metal binding to the Cys29 residue in the enzyme active site which is in close proximity to the nitroxoline binding site. The binding mode of metalloinhibitors was proposed on the basis of an active-site titration and protection-from-inactivation assays[36] as well as docking simulations.[37] Additionally, ruthenium complexes can be used also for caging of protease inhibitors and it was also found that their light activation enables kinetic control of protease activity.[41−43]

To continue with the exploration of the chemical space of the 5-nitroquinoline scaffold, we decided to introduce metal-containing fragments to positions 1 and 8 of the nitroxoline ring (Figure 1; right). Herein, we present the synthesis, characterization, and biological evaluation of 10 new and 1 previously reported[44] organoruthenium complex with the parent ligand nitroxoline and five nitroxoline-derived inhibitors of catB.

RESULTS AND DISCUSSION

Synthesis and Characterization. The synthesis of the parent ruthenium nitroxoline complex **1a** (Table 1) was reported earlier by Thai et al.,[44] but we have modified the method as described below to obtain simple high-yield procedures. In the case of complex **1a**, we followed the previously reported simplified and high-yield synthetic route for the preparation of the clioquinolato complex with in situ deprotonation of the ligand with sodium methoxide in a 1/1 $CHCl_3$/MeOH mixture, removal of the byproduct NaCl from a DCM solution, and precipitation of the product with the addition of *n*-hexane.[28] The bromido, iodido, and azido analouegs **1b−d** were, however, synthesized using acetone as a solvent to allow the removal of NaCl directly from the reaction mixture and facilitate precipitation by addition of *n*-hexane as, when precipitating from a DCM solution, we often observed the formation of oily products. In the case of the synthesis of complexes with 7-substituted nitroxolines, this approach was unsuccessful. It often resulted in mixtures of several ruthenium-containing species, most likely due to the coordinating ability of the fragments at position 7 of the hq ligand.

In the crude reaction mixture of complex **2a**, we observed a few crystals of distinctly different color and morphology and were able to determine the crystal structure of the secondary species **2a′**, which proved to be a dimer. In this compound, the new bridging dianionic ligand $\mathbf{L_2}$ was bound to one ruthenium ion through the N1 and O8 atoms and to the second ruthenium ion through the carboxylate oxygen, which replaced the dissociated chlorido ligand (see the Supporting Information). Attempts to isolate this compound in pure form have been unsuccessful as yet. In order to achieve even milder reaction conditions, we reacted the ruthenium precursors with the ligands without the addition of a base. The reactions resulted in pure compounds with high reaction yields where, interestingly, ligands $\mathbf{L^2H}$ and $\mathbf{L^6H}$ were bound in zwitterionic form with the deprotonated hydroxyl group and the protonated amine group on the substituent in position 7 resulting in PF_6^- salts of the orresponding cationic complexes **2a**,**b** and **6a**. On the other hand, ligands $\mathbf{L^3}$−$\mathbf{L^5}$ were bound in anionic form, resulting in neutral complexes. This was confirmed by both CHN elemental analysis and the presence of a sharp signal in the IR spectrum at approximately 815−835 cm^{-1} corresponding to the vibrations of the hexafluoridophosphate anion.

We were able to obtain crystals suitable for X-ray structure analysis of complexes **1a, 1c**, and **2a′** by slow evaporation of 1/1 DCM/*n*-hexane solutions. The structures (Figure 2) confirm the binding mode and overall structural properties of previously known organoruthenium complexes with 8-hydroxyquinolinato complexes.[28,29,31,44−47]

The solution stability of **1a** was monitored by ^{1}H NMR in DMSO-d_6 and D_2O. The spectra remained unchanged for 3 and 5 days (Figures S1 and S2), respectively, which conforms with the findings of Kubanik et al.,[45] where an in-depth study of solution stability was performed including pD-dependence experiments. Their study revealed the stability of ruthenium hydroxyquinolinato complexes in DMSO-d_6 solutions, a quick aquation step with the substitution of halido ligand by D_2O molecules in aqueous media, and the stability of the complexes in highly acidic media comparable to the stomach environment.

Inhibition of catB Activity Determined by Enzyme Kinetics. All of the prepared organoruthenium complexes were first evaluated in initial enzyme kinetic assay to determine their relative inhibition of catB endopeptidase and exopeptidase activities (Table 2). Relative inhibition is expressed as a percentage of the decrease in reaction velocity in the presence of an inhibitor in comparison to the reaction velocity in the absence of an inhibitor. For that purpose, the specific substrates Z-Arg-Arg-7-amido-4-methylcoumarin (Z-Arg-Arg-AMC) and 2-aminobenzoyl (Abz)-Gly-Ile-Val-Arg-Ala-Lys-(Dnp)-OH for catB endopeptidase and exopeptidase activities were used, respectively. CatB cleaves protein substrates as an endopeptidase in the middle ofthe polypeptide chain at neutral pH, when the salt bridges are disrupted and the occluding loop is in an open conformation, which enables the access of such substrates to the active site of the enzyme. On the other hand, at lower pH when the occluding loop is attached to the body of the enzyme, access of larger substrates is prevented. CatB then acts as an exopeptidase (peptidyldipeptidase) by cleaving two amino acid residues at the C-terminal end of a polypeptide chain. The free −COOH group at the Lys residue of the

DOI: 10.1021/acs.inorgchem.9b01882
Inorg. Chem. 2019, 58, 12334−12347

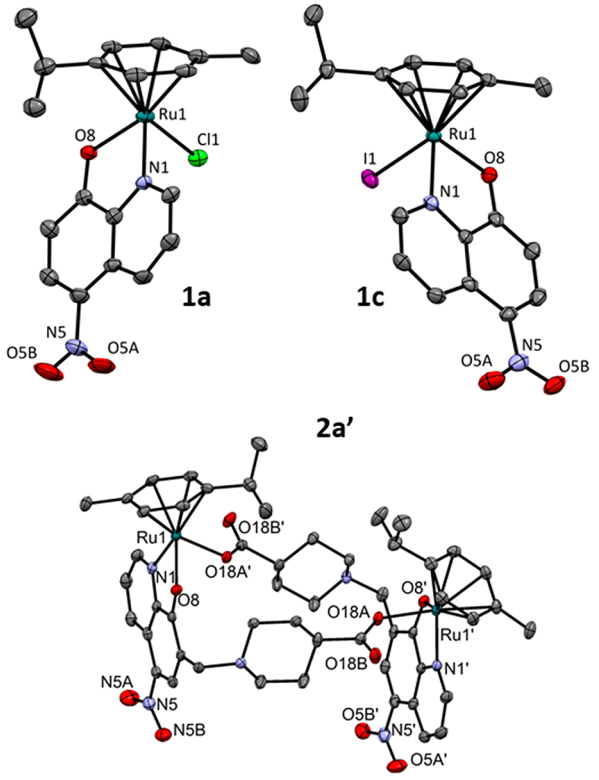

Figure 2. (left to right) Crystal structures of organoruthenium complexes with nitroxoline **1a**,**c** and **2a**′. The ellipsoids are drawn at the 35% probability level, and the hydrogen atoms are omitted. Detailed crystallographic data are given in Table S1 in the Supporting Information.

exopeptidase substrate (Abz)-Gly-Ile-Val-Arg-Ala-Lys(Dnp)-OH mimics the C-terminal end of a polypeptide chain.

Next, derivatives that exhibited relative inhibition of 20% or more were characterized in detail by determining their inhibition constants and modes of inhibition (Table 2). Four organoruthenium complexes with nitroxoline (**1a**−**d**) differed in the reactivity of the monodentate ligand, as the chlorido ligand in the parent Ru-nx complex (**1a**) was replaced by a bromido, iodido, or azido ligand in compounds **1b**−**d**, respectively. These four monodentate ligands are known to possess increasingly slow substitution/aquation rates,[48] which are known to affect the biological activity of organoruthenium compounds, although to a minor extent.[31,32,45,46] According to the obtained constants of inhibition, the change in monodentate ligand affected the inhibitory properties of complexes against catB. Generally, the formation of organoruthenium complexes with nitroxoline and its derivatives resulted in increased inhibition of catB exopeptidase activity in comparison with the ligands alone (Table 2).[15] In the case of **nxH** (**L**^{1}**H**) complexes, the most potent inhibitor of catB exopeptidase activity was **1d**, with an 8-fold increase in inhibition in comparison to **nxH**. Moreover, a change in mode of inhibition for complexes **1d** and the next most potent inhibitor of catB exopeptidase activity, **1a** (5-fold increase of inhibition), was observed, exhibiting a mixed type of inhibition with a predominantly uncompetitive component, in comparison to the noncompetitive mode observed for **nxH**. On the other hand, inhibition of endopeptidase activity was affected to a lesser extent by ruthenium complexes in comparison to the inhibition by **nxH** alone.[15] Here, only compound **1d** with the azido group as the monodentate ligand the improved inhibition of catB endopeptidase activity in comparison with **nxH**. Similar to the case for **nxH**, which is a mixed type inhibitor with a predominantly uncompetitive component, complexes **1c**,**d** with lower constants of inhibition showed an uncompetitive mode of inhibition, while **1a**,**b** with slightly higher K_i values showed a noncompetitive type of inhibition. A

Table 2. Relative Inhibition, Inhibition Constants, and Mechanisms of Inhibition of Cathepsin B Endopeptidase and Exopeptidase Activities

	cathepsin B					
	Z-RR-AMC			Abz-GIVRAK(Dnp)-OH		
compound	R_i (%)	K_i[a] (μM)	K_i′[b] (μM)	R_i (%)	K_i (μM)	K_i′ (μM)
nxH; **L**^{1}**H**[g]		154.4 ± 26.7[c]	39.5 ± 2.8[c]		271.8 ± 11.2[d]	
1a	44.3 ± 1.7	77.9 ± 16.1[d]		22.5 ± 4.7	126.2 ± 16.9[c]	51.2 ± 22.7[c]
1b	27.2 ± 2.0	94.7 ± 1.7[d]		12.0 ± 7.4	224.6 ± 2.1[d]	
1c	24.9 ± 2.3		55.9 ± 4.0[e]	46.6 ± 12.5	64.4 ± 5.2[d]	
1d	32.9 ± 1.6		21.5 ± 0.4[e]	31.0 ± 6.2	126.7 ± 43.1[c]	32.1 ± 16.3[c]
L^{2}**H**[g]		92.9 ± 1.9[c]	66.5 ± 0.4[c]		347.8 ± 16.1[d]	
2a	21.6 ± 2.1	n.d.		4.2 ± 7.1	n.d.	
2b	22.2 ± 1.1	140.8 ± 29.9[d]		14.6 ± 0.5	129.8 ± 20.1[d]	
L^{3}**H**[g]		118.8 ± 4.2[d]			199.7 ± 11.2[d]	
3a	17.2 ± 1.5	104.4 ± 28.7[d]		2.8 ± 1.4	117.6 ± 5.6[d]	
3c	17.2 ± 0.3	n.d.		7.3 ± 3.2	n.d.	
L^{4}**H**[g]		129.8 ± 3.5[d]			116 ± 2.4[f]	
4a	22.3 ± 3.1	89.0 ± 2.9[d]		24.8 ± 2.2	73.2 ± 2.0[c]	149.9 ± 3.0[c]
L^{5}**H**[h]		126 ± 40[h]	76 ± 16[h]		172 ± 16[h]	
5a	18.7 ± 2.5	n.d.		13.5 ± 6.0	n.d.	
L^{6}**H**[g]		117.8 ± 3.1[g]			108.2 ± 13.4[g]	
6a	11.7 ± 0.4	n.d.		0.4 ± 0.3	n.d.	

[a]The dissociation constant for the dissociation of enzyme−inhibitor complex. [b]The dissociation constant for dissociation of the enzyme−substrate-inhibitor complex. [c]Mixed inhibition. [d]Noncompetitive inhibition. [e]Uncompetitive inhibition. [f]Competitive inhibition; n.d. = not determined. [g]Data reported in ref 15. [h]Data reported in ref 18.

DOI: 10.1021/acs.inorgchem.9b01882
Inorg. Chem. 2019, 58, 12334−12347

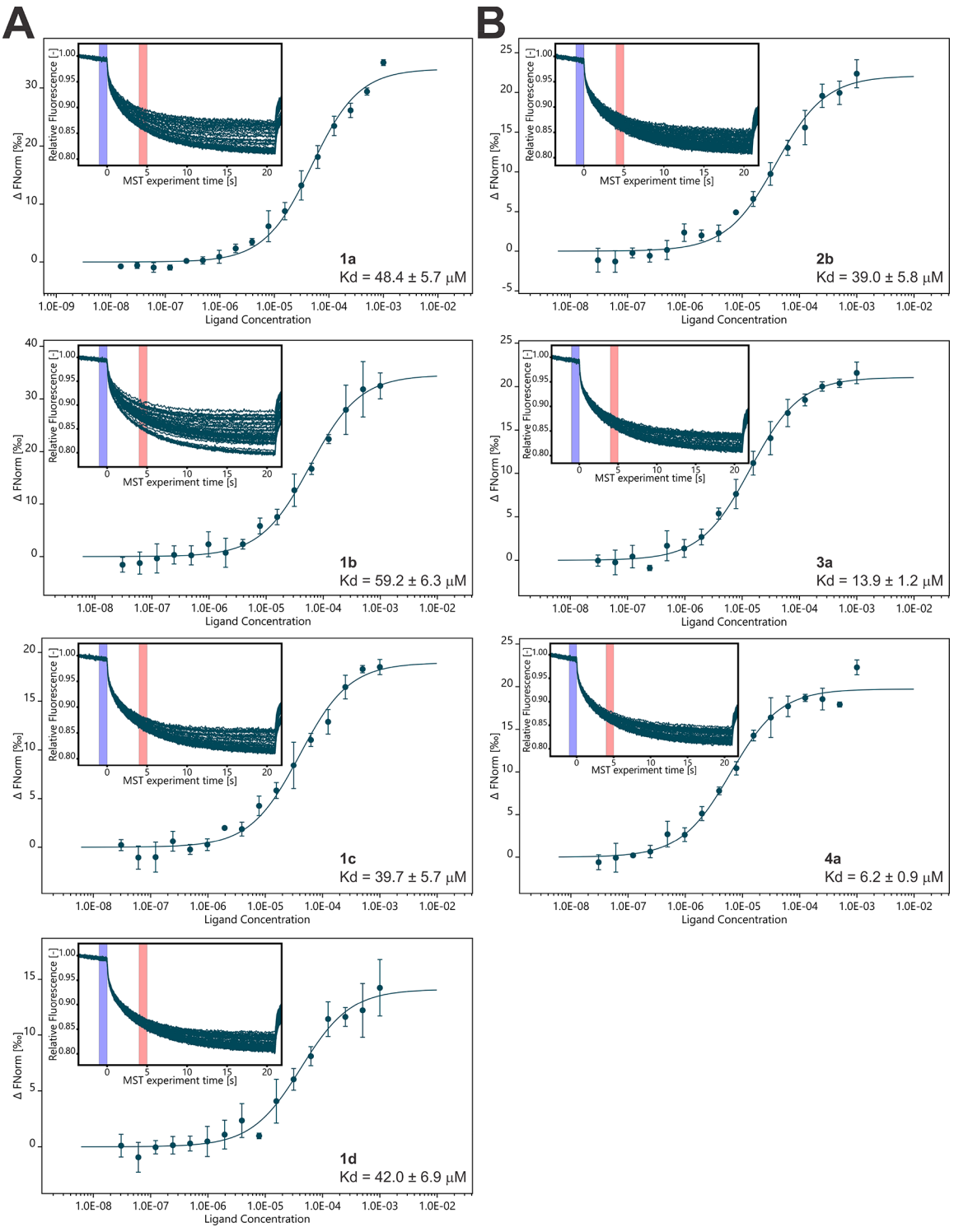

Figure 3. MST affinity analyses of interactions of organoruthenium complexes with cathepsin B: (A) nitroxoline-ruthenium complexes (compounds **1a**–**d**) and (B) ruthenium complexes with nitroxoline derivatives (compounds **2b**, **3a**, and **4a**). Data are presented as K_d values calculated form normalized fluorescence (F_{norm}) as a function of compound concentration from three independent experiments (mean ± STDEV). The ligand concentration is presented in mol/L. The inserts show MST traces used for calculation of F_{norm} for the construction of sigmoid dose–response curves.

similar effect on catB inhibition was observed also for ruthenium complexes with nitroxoline derivatives. Again, the formation of ruthenium complexes predominantly improved the inhibition of catB exopeptidase activity in comparison with free ligands $\mathbf{L^2H}$–$\mathbf{L^6H}$ (at most 2.7-fold for **2b**) and only influenced the endopeptidase activity to a lesser extent (Table 2). This observation is also in line with our previous findings, where we showed that larger substituents are preferred for improved inhibition of catB exopeptidase activity.[18,19]

Binding Affinity of Organoruthenium Complexes on catB As Determined Using MST. To further confirm the binding affinity of ruthenium complexes with catB, we applied

DOI: 10.1021/acs.inorgchem.9b01882
Inorg. Chem. 2019, 58, 12334–12347

microscale thermophoresis (MST). MST is highly sensitive biophysical method that enables the quantification of binding affinity between a ligand and its fluorescently labeled target on the basis of changes in directed movement of a fluorescently labeled molecule in a temperature gradient.[49,50] To the best of our knowledge, we are aware of only another study where MST was used to study the interactions of metal complexes with their protein targets.[51]

From dose−response curves and MST traces (Figure 3) we can confirm the binding of compounds **1a−d**, **2b**, **3a** and **4a** to catB. The obtained average dissociation constants (K_d) for ruthenium complexes with nitroxoline (**1a−d**) are in the same concentration range as their constants of inhibition determined by a enzyme kinetic assay and only minor differences in K_d values between complexes with different monodentate ligands can be seen (Figure 3A). In contrast, for ruthenium complexes with nitroxoline derivatives **2b**, **3a**, and **4a** the average K_d values were lower in comparison to the K_i values for endopeptidase activity inhibition obtained using fluorescent substrates in a enzyme kinetics assay: i.e. 14.4-fold (6.2 ± 0.9 μM) for **4a**, 7.5-fold (13.9 ± 1.2 μM) for **3a**, and 3.6-fold (39.0 ± 5.8 μM) for **2b** (Figure 3B). Among them, similarly as in the enzyme kinetic assay, the K_d value was the lowest for **4a** and the highest for **2b**. The deviation between dissociation and inhibition constants can be explained by differences in experimental setup between two methods: namely, the MST is a binding study, whereas the enzyme kinetics measurements evaluate the ability of an enzyme to degrade a fluorescently labeled substrate.

Effect on the Viability of Tumor Cells. Next, we evaluated the complexes in cell-based in vitro assays of tumor invasion and degradation of the extracellular matrix (ECM). To be able to distinguish effects caused by specific mechanisms in functional assays and not only effects due to triggering cell cytotoxicity, we first assessed the cytotoxic effect of ruthenium complexes on MCF-10A neoT cells and selected the concentrations of compounds that did not decrease cell viability for further studies. MCF-10A neoT cells express high levels of proteolytically active catB[17] and are therefore used as a model cell line for functional assays. Using the MTS assay, we evaluated the cytotoxic effect of ruthenium complexes after 72 h treatment in the concentration range from 250 nM to 5 μM (Figure 4). On the basis of the obtained results, a concentration of 1.25 μM was selected as noncytotoxic for ruthenium complexes **1a**,**b**,**d** (Figure 4A) and **2b**, **3a**, and **4a** (Figure 4B). Only ruthenium nitroxoline complex **1c** bearing the iodido ligand was more cytotoxic; therefore, to avoid an apparent decrease in the tumor cell invasion as a result of the higher cytotoxicity of the compound, the concentration 500 nM was used in a tumor cell invasion assay for **1c** (Figure 4A).

The Ruthenium Complexes Impair Degradation of ECM by Tumor Cells. During cancer progression, the degradation of ECM is one of the most crucial processes enabling tumor cell migration, invasion, and metastasis. In this process, catB was shown to substantially contribute, acting either extracellularly or intracellularly. Extracellularly, ECM is degraded by secreted and membrane-associated catB, while intracellular degradation of ECM takes place within lysosomes following endocytosis of partially degraded components of ECM.[1,10,52] To investigate the effect of ruthenium complexes on the degradation of ECM, we used DQ-collagen type IV and MCF-10A neoT cells that were shown to degrade DQ-collagen type IV both intracellularly and extracellularly.[17] Collagen type

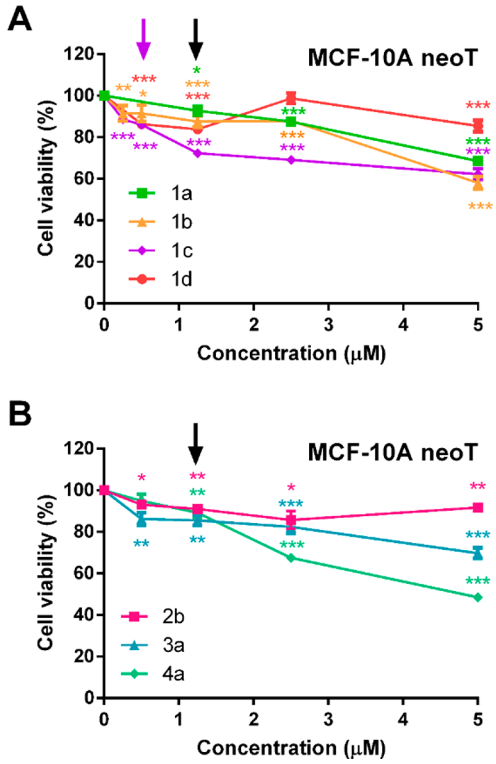

Figure 4. The effect of ruthenium complexes on MCF-10A neoT cell viability as determined by an MTS assay. MCF-10A neoT cells were treated with increasing concentrations of (A) nitroxoline-ruthenium complexes (compound **1a−d**) and (B) ruthenium complexes with nitroxoline derivatives (compounds **2b**, **3a**, and **4a**) for 72 h before MTS reagent was added. Data are presented as percentage of viable cells from at least two independent experiments (mean ± SEM) in the presence of the inhibitor in comparison to DMSO, which was used as a control. Black arrows denote concentrations of compounds selected for further cell-based functional assays, and the purple arrow denotes the selected concentration of compound **1c**. The experiments were performed in quadruplicate. *P < 0.05, **P < 0.01, ***P < 0.001.

IV is a major component of the ECM that can be tagged with fluorescein, and the proteolytic cleavage gives rise to bright green fluorescence (Figure 5A,D). Degradation of DQ-collagen IV was quantified by flow cytometry for intracellular degradation and by spectrofluorimetry for extracellular degradation (Figure 5). Among the ruthenium complexes with the parent nitroxoline ligand (**1a−d**) we observed a general trend in both intra- and extracellular DQ-collagen IV degradation rates in dependence on the monodentate ligand ($Cl^- > Br^- > N_3^- \geq I^-$). Complexes **1a**, **1b**, **1d**, and **1c** at a concentration of 1.25 μM reduced intracellular degradation by 45 ± 2%, 40 ± 3%, 31 ± 2%, and 21 ± 2%, respectively (Figure 5B). A similar pattern was observed also for extracellular degradation that was reduced by 35 ± 2%, 26 ± 3%, 21 ± 3%, and 19 ± 2% for complexes **1a**, **1b**, **1d**, and **1c** at a concentration of 1.25 μM, respectively (Figure 5C). Despite the reduction in cell viability for complex **1c** (Figure 5A) we included this concentration in the assays, as ECM degradation experiments were performed at shorter time points in comparison to viability assays. In addition, when intracellular degradation was monitored by flow cytometry, propidium iodide was added to exclude dead cells and only effects in viable cells were measured. At a lower concentration (0.5 μM) **1c** displayed a less pronounced effect on DQ-collagen IV

DOI: 10.1021/acs.inorgchem.9b01882
Inorg. Chem. 2019, 58, 12334−12347

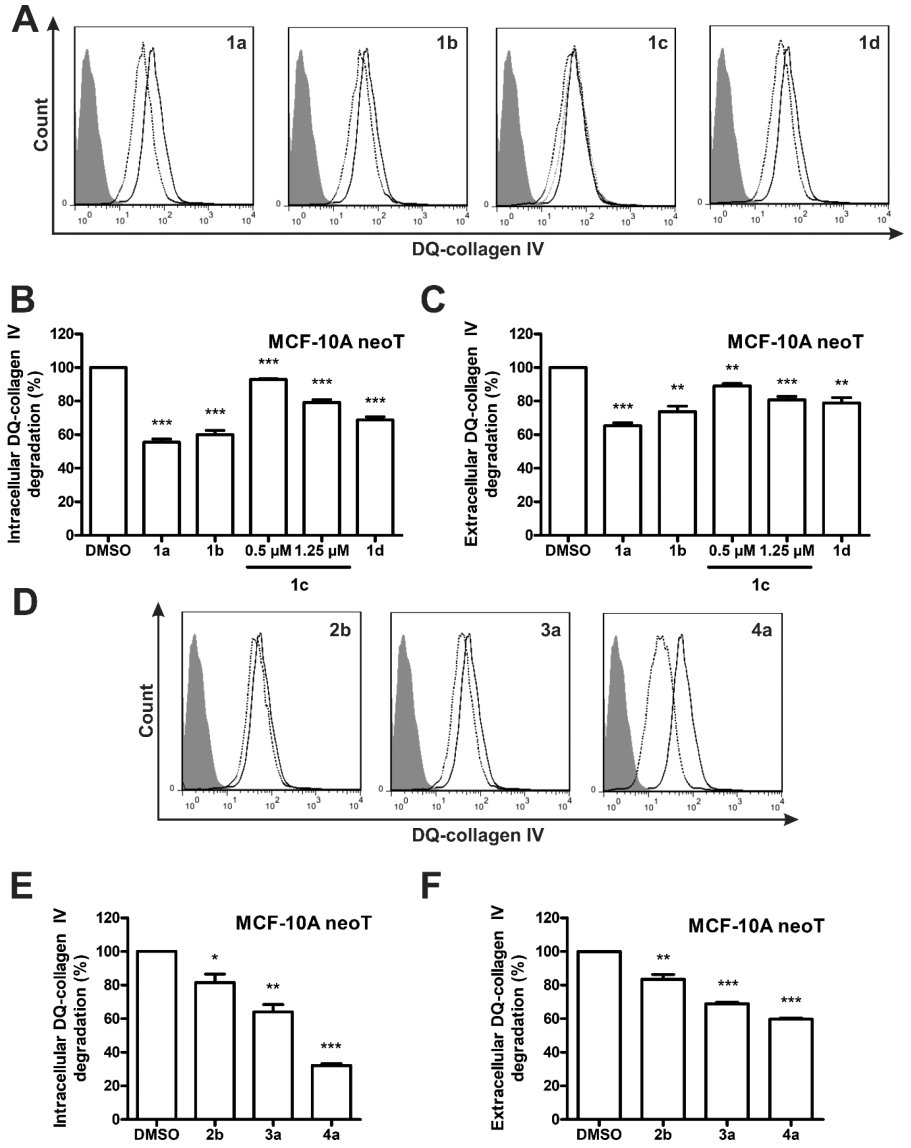

Figure 5. Ruthenium complexes impair intracellular and extracellular degradation of ECM by MCF-10A neoT cells. (A, D) Intracellular DQ-collagen IV degradation by MCF-10A neoT cells (6×10^4) after treatment with DMSO (solid black line) or the respective compound (dotted black line or dotted gray line for 0.5 μM for **1c**) was monitored using flow cytometry: (A) nitroxoline-ruthenium complexes (compounds **1a**–**d**) used in concentrations of 1.25 and 0.5 μM for **1c**; (D) ruthenium complexes with nitroxoline derivatives (compounds **2b**, **3a** and **4a**) used in concentrations of 1.25 μM. Gray histograms denote unlabeled cells. (B, E) Reduction of intracellular DQ-collagen IV in the presence of DMSO or suitable compound for (B) nitroxoline-ruthenium complexes (1.25 and 0.5 μM **1c**) and (E) ruthenium complexes with nitroxoline derivatives (1.25 μM) as assayed by flow cytometry. Data are presented as means ± SEM (n = 3), and experiments were performed in duplicate. (C, F) Extracellular degradation of DQ-collagen IV by MCF-10A neoT cells (5×10^4) in the presence of DMSO or the respective compound for (C) nitroxoline-ruthenium complexes (1.25 and 0.5 μM **1c**) and (F) ruthenium complexes with nitroxoline derivatives (1.25 μM) was analyzed by monitoring the fluorescence intensity of the extracellular degradation product using spectrofluorimetry. Data are presented as means ± SEM (n = 3). *P < 0.05, **P < 0.01, ***P < 0.001.

degradation (Figure 5B,C). The most potent inhibitor of both intra- and extracellular DQ-collagen IV degradation was complex **1a**, bearing the chlorido ligand as the leaving group.

Furthermore, ruthenium complexes with nitroxoline derivatives **2b**, **3a**, and **4a** also significantly impaired DQ-collagen IV degradation, both intracellularly and extracellularly. The most potent inhibitor was **4a**, which reduced intracellular and extracellular degradation by 68 ± 1% and 40 ± 1%, respectively (Figure 5E), whereas **3a** and **2b** reduced intracellular degradation by 36 ± 4% and 18 ± 5%, respectively, and extracellular degradation by 31 ± 1% and 17 ± 3%, respectively (Figure 5F). These results also confirm our previous observation that both intra- and extracellular DQ-collagen IV degradation is dependent on the monodentate ligand, as both complexes with nitroxoline derivatives bearing the chlorido ligand as the leaving group (**3a** and **4a**) were more potent inhibitors in comparison to **2b** bearing the bromido ligand. Moreover, the results obtained for ruthenium complexes with nitroxoline derivatives also point out the importance of the main ligand in the ruthenium complexes and its potency for catB inhibition, as compounds **1a**, **3a** and **4a**, all bearing the chlorido ligand as the leaving group, have different potencies for inhibition of ECM degradation, where a higher

DOI: 10.1021/acs.inorgchem.9b01882
Inorg. Chem. 2019, 58, 12334−12347

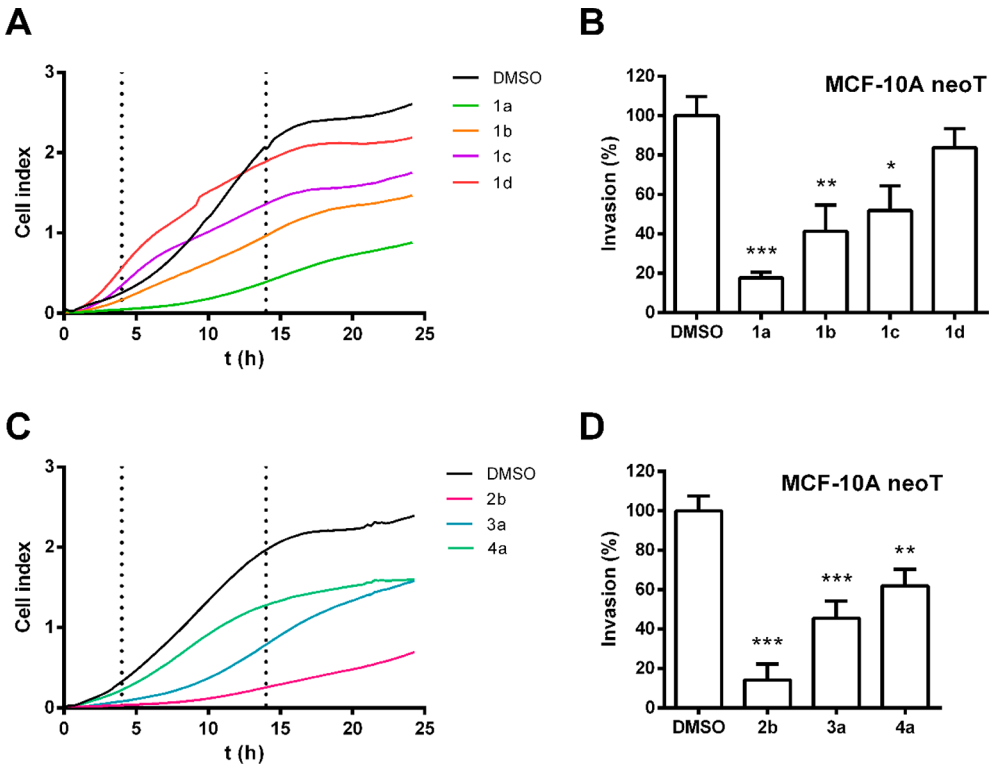

Figure 6. Ruthenium complexes impair invasion of MCF-10A neoT cells. (A, C) MCF-10A neoT cells (3×10^4) were seeded on top of Matrigel (1 mg/mL) coated upper compartments of CIM-plate 16. DMSO (0.05%) or the respective compound (A) nitroxoline-ruthenium complex (1.25 μM for compounds **1a**, **1b**, and **1d** or 0.5 μM for compound **1c**) and (C) ruthenium complexes with nitroxoline derivatives (1.25 μM for compounds **2b**, **3a**, and **4a**) was added to the growth medium in the upper and lower compartments of the CIM-plate 16. Cell invasion was monitored continuously for 72 h by measuring impedance data (reported as CI) using the xCELLigence system. (B, D) Slopes (1/h) in the time interval between 4 and 14 h correlated the ability of the cells to invade and were used to calculate the percentage of invasion (%) for (B) nitroxoline-ruthenium complexes and (D) ruthenium complexes with nitroxoline derivatives, presented as means ± SEM (n = 2). The experiments were performed in triplicate. *P < 0.05, **P < 0.01, ***P < 0.001.

binding affinity for catB resulted in an improved potency for inhibition of ECM degradation.

The Ruthenium Complexes Reduce Tumor Cell Invasion at Noncytotoxic Concentrations. To further characterize the antitumor characteristics of selected complexes, their effect on tumor cell invasion was evaluated. For this purpose, we continuously monitored the invasion of MCF-10A neoT cells through Matrigel, a model of ECM, using the xCELLigence system (Figure 6A,C). The system follows tumor cell invasion during the whole course of the experiment by continuously measuring the impedance, expressed as cell index (CI), across the microelectrodes integrated in the membrane separating the top and bottom compartments of the CIM (cell invasion and migration) plate 16. As shown in Figure 6A,B, low noncytotoxic concentrations of **1a**–**d** which bear different monodentate ligands impaired tumor cell invasion to different extents. The most potent was complex **1a**, which significantly reduced tumor invasion of MCF-10A neoT cells by 82 ± 3%, followed by **1b** with a 59 ± 13% reduction in invasion (both at a concentration of 1.25 μM), and **1c** with a reduction of 48 ± 13% at 0.5 μM (Figure 6B). The invasion of MCF-10A neoT cells in the presence of **1d** was not significantly impaired (Figure 6B). In line with the data obtained for degradation of ECM, these data show that complexation of nitroxoline with an organoruthenium moiety further improves in vitro inhibition of tumor cell invasion. In comparison to ECM degradation using DQ-collagen IV, tumor cell invasion is a more complex process involving the coordinated action of several peptidases. Therefore, inhibition of one of them could have an effect on other peptidases and their contribution to the tumor invasion. That could be an explanation for the differences in some of the compounds, such as **1d**, between the ECM degradation assay and the invasion assay. Moreover, compensational mechanisms observed between related cathepsins could be differently affected by the complexes.[53,54] The process of tumor invasion also involves the action of other tumor-promoting molecules that could also serve as therapeutic targets. In addition to affecting catB activity, **nxH** was identified to impair tumor progression by inhibition of other molecular targets, such as methionine aminopeptidase type 2,[55] sirtuin,[55] Foark head box M1 (FoxM1) signaling,[56] and the bromodomain-containing protein 4 (BRD4) member of the BET family.[57] Additionally, **nxH** inhibits tumor progression by inducing apoptosis.[58−60] Therefore, the possible effect of complexes **1a**–**d** on other targets involved in tumor invasion cannot be excluded. In addition, ruthenium complexes with nitroxoline derivatives **2b**, **3a**, and **4a** also significantly impaired invasion of MCF-10A neoT cells (Figure 6C,D). In this group, compound **2b** was the best inhibitor with 86 ± 8% inhibition of cell invasion, whereas **3a** and **4a** decreased this process by 54 ± 8% and 38 ± 8%, respectively (Figure 6D). Again, differences between the ECM degradation assay and the cell invasion assay can be observed, probably as a result of the aforementioned processes. Also, nitroxoline derivatives with different substituents can affect the selectivity for catB affecting the activity of other cathepsins in addition to catB.

DOI: 10.1021/acs.inorgchem.9b01882
Inorg. Chem. 2019, 58, 12334−12347

Taken together, we have demonstrated here that new ruthenium complexes in noncytotoxic 1.25 μM concentrations significantly decreased tumor cell invasion by inhibition of tumor-promoting peptidase catB. In addition to catB, the compounds may affect also other specific targets involved in cell invasion.

CONCLUSIONS

By synthesizing 11 ruthenium compounds bearing either the clinical agent nitroxoline (**nxH**) or its potent cathepsin B (catB) inhibiting derivatives, we have demonstrated that organoruthenation of the lead **nxH** scaffold is a viable strategy for obtaining highly effective catB inhibitors, the agents that efficiently reduce tumor cell invasion. Using enzyme kinetics and MST, we showed that the novel metallodrugs inhibit both endo- and exopeptidase activity of catB and significantly impair the processes of tumor progression such as degradation of ECM and tumor cell invasion.

The present study provides us with several insights into the influence of the chemical structure on the pharmacological properties of this class of compounds. As a general trend, we observed an improvement in catB inhibition, lowering of ECM degradation, and reduction of tumor cell invasion by metallodrugs in comparison with free ligands. Moreover, we can observe a clear correlation between ECM degradation and reduction of tumor cells with the reactivity of the monodentate leaving ligand, where the most reactive chlorido complex **1a** showed the strongest effect (**1a** > **1b** > **1c** ≈ **1d**).

EXPERIMENTAL SECTION

Materials and Methods. $[(\eta^6\text{-}p\text{-cymene})RuCl(\mu\text{-}Cl)]_2$ (**P1**) was purchased from Strem Chemicals, nitroxoline (**nxH**), $[(\eta^6\text{-}p\text{-cymene})\text{-}RuI(\mu\text{-}I)]_2$ (**P3**), and the solvents were obtained from Sigma-Aldrich. All of the materials were used as received. The bromide precursor $[(\eta^6\text{-}p\text{-cymene})RuBr(\mu\text{-}Br)]_2$ (**P2**) and $[(\eta^6\text{-}p\text{-cymene})RuCl(\mu\text{-}N_3)]_2$ (**P4**) were synthesized by reacting precursor **P1** with excess KBr and NaN_3, respectively, according to published procedures.[61,62] Nitroxoline-based ligands were prepared according to the published procedure.[15,20] ^{1}H NMR spectra were recorded on a Bruker Avance III 500 spectrometer at room temperature and 500.10 MHz by using TMS as an internal standard. Infrared spectra were recorded with a PerkinElmer Spectrum 100 FTIR spectrometer, equipped with a Specac Golden Gate Diamond ATR as a solid sample support. UV−vis spectra were collected on a PerkinElmer LAMBDA 750 UV/vis/near-IR spectrophotometer. Elemental analyses were recorded using a PerkinElmer 2400 II instrument (CHN), and HRMS were measured on an Agilent 6224 Accurate Mass TOF LC/MS instrument. X-ray diffraction data were collected on an Oxford Diffraction SuperNova diffractometer with an Mo/Cu microfocus X-ray source (Kα radiation, λ_{Mo} = 0.71073 Å, λ_{Cu} = 1.54184 Å) with mirror optics and an Atlas detector at 150(2) K. The structures were solved in Olex^2 graphical user interface[63] by direct methods implemented in SHELXT and refined by a full-matrix least-squares procedure based on F^2 using SHELXL.[64] All non-hydrogen atoms were refined anisotropically. The hydrogen atoms were placed at calculated positions and treated using appropriate riding models. The crystal structures have been submitted to the CCDC and have been allocated the deposition numbers 1909464−1909466.

Syntheses and Characterization. *$[Ru(\eta^6\text{-}p\text{-cymene})Cl(nx)]$ (**1a**).* The synthesis and characterization of complex **1a** were previously reported.[44] Here, we report an improved reliable high-yield synthetic procedure. A 40.0 mg portion of the ruthenium chlorido precursor (**P1**, 0.0650 mmol), 24.9 mg of **nxH** (1.00 equiv, 0.130 mmol), and 7.00 mg of NaOMe (0.130 mmol) were dissolved in 20 mL of a 1/1 mixture of $CHCl_3$ and MeOH. The solution was refluxed for 2 h and the solvent evaporated. The crude product was redissolved in DCM and the solution filtered to remove the precipitated NaCl. The filtrate was concentrated on a rotary evaporator and precipitated by the addition of *n*-hexane. The orange precipitate was collected by filtration and washed with *n*-hexane (η = 90%).

^{1}H NMR (500 MHz, $CDCl_3$): δ 9.51 (d, J = 8.8 Hz, 1H, C^2*H*); 9.01 (d, J = 4.6 Hz, 1H, C^4*H*); 8.56 (d, J = 9.3 Hz, 1H, C^6*H*); 7.63 (dd, J = 8.9, 4.8 Hz, 1H, C^3*H*); 6.90 (d, J = 9.3 Hz, 1H, C^7*H*); 5.68 (d, J = 5.9 Hz, 1H, Ar-*H* cym); 5.57 (d, J = 5.8 Hz, 1H, Ar-*H* cym); 5.50 (d, J = 5.9 Hz, 1H, Ar-*H* cym); 5.39 (d, J = 5.8 Hz, 1H, Ar-*H* cym); 2.81 (sept, J = 6.8 Hz, 1H, Ar-C*H*$(CH_3)_2$ cym); 2.33 (s, 3H, Ar-C*H*$_3$ cym); 1,20 (dd, J = 6.9, 2.7 Hz, 6H, Ar-CH(C*H*$_3)_2$ cym). Selected IR resonances (cm^{-1}, ATR): 2969, 1595, 1566, 1510, 1481, 1464, 1385, 1287, 1278, 1189, 1149, 860, 820, 788, 742. Anal. Calcd for $C_{19}H_{19}ClN_2O_3Ru$: C, 49.62; H, 4.16; N, 6.09. Found: C, 49.65; H, 3.89; N, 5.82. UV/vis (λ, nm (ε; L mol^{-1} cm^{-1})) c = 1 × 10^{-4} mol L^{-1}, MeOH: 268 (15000), 350 (6500), 430 (14100), 450 (13900). ESI-HRMS (CH_3CN) m/z (observed [M − Cl]$^+$, [M + H]$^+$, [2 M − Cl]$^+$ (expected)): 425.0439 (425.0439) 461.0198 (461.0206), 885.0577 (885.0567).

*$[Ru(\eta^6\text{-}p\text{-cymene})Br(nx)]$ (**1b**).* A 40.0 mg portion of the ruthenium bromido precursor (**P2**, 0.0500 mmol) and 19.0 mg of **nxH** (1.00 equiv, 0.100 mmol), and 5.4 mg of NaOMe (0.100 mmol) were suspended in 20 mL of acetone and stirred at room temperature for 3 h. The precipitate was filtered off, the deep orange filtrate was concentrated on a rotary evaporator, and the product was precipitated by the addition of *n*-hexane. The orange precipitate was collected by filtration and washed with *n*-hexane (η = 90%).

^{1}H NMR (500 MHz, $CDCl_3$): δ 9.51 (d, J = 8.7 Hz, 1H, C^2*H*), 8.98 (s, 1H, C^4*H*), 8.56 (d, J = 9.3 Hz, 1H, C^6*H*), 7.62 (d, J = 4.9 Hz, 1H, C^3*H*), 6.90 (d, J = 9.3 Hz, 1H, C^7*H*), 5.64 (d, J = 5.3 Hz, 1H, Ar-*H* cym), 5.54 (dd, J = 22.1, 5.1 Hz, 2H, Ar-*H* cym), 5.40 (d, J = 4.9 Hz, 1H, Ar-*H* cym), 2.88 (sept, J = 13,5, 6.7 Hz, 1H, Ar-C*H*$(CH_3)_2$ cym), 2.38 (s, 3H, Ar-C*H*$_3$ cym), 1,22 (d, J = 6.8 Hz, 6H, Ar-CH(C*H*$_3)_2$ cym). Selected IR resonances (cm^{-1}, ATR): 2966, 1595, 1564, 1505, 1476, 1464, 1412, 1384, 1271, 1180, 1142, 1103, 810, 781, 745. Anal. Calcd for $C_{19}H_{19}BrN_2O_3Ru$: C, 45.25; H, 3.80; N, 5.55. Found: C, 45.16; H 3.66; N, 5.43. UV/vis (λ, nm (ε; L mol^{-1} cm^{-1})) c = 1 × 10^{-4} mol L^{-1}, $CHCl_3$: 276 (18900), 372 (9900), 455 (20900), 478 (20200). ESI-HRMS (CH_3CN) m/z (observed [M − Br]$^+$, [M + H]$^+$ (expected)): 419.0466 (419.0466), 500.9703 (498.9728).

*$[Ru(\eta^6\text{-}p\text{-cymene})I(nx)]$ (**1c**).* A 49.0 mg portion of the ruthenium iodido precursor (**P3**, 0.0500 mmol), 19.0 mg of **nxH** (1.00 equiv, 0.100 mmol), and 5.4 mg of NaOMe (0.100 mmol) were suspended in 20 mL of acetone and stirred at room temperature for 3 h. The precipitate was filtered off, the deep red filtrate was concentrated on a rotary evaporator, and the product was precipitated by the addition of *n*-hexane. The dark red precipitate was collected by filtration and washed with *n*-hexane (η = 92%).

^{1}H NMR (400 MHz, $CDCl_3$): δ 9.52 (d, J = 8.9 Hz, 1H, C^2*H*), 8.96 (d, J = 3,9 Hz, 1H, C^4*H*), 8.58 (d, J = 9.3 Hz, 1H, C^6*H*), 7.61 (dd, J = 8.9, 5.0 Hz, 1H, C^3*H*), 6.90 (d, J = 9.3 Hz, 1H, C^7*H*), 5.68−5.57 (m, 3H, Ar-*H* cym), 5.42 (d, J = 5.8 Hz, 1H, Ar-*H* cym), 2.98 (sept, J = 13,8, 6.9 Hz, 1H, Ar−C*H*$(CH_3)_2$ cym), 2.46 (s, 3H, Ar-C*H*$_3$ cym), 1,27 (dd, J = 6.9, 1,6 Hz, 6H, Ar-CH(C*H*$_3)_2$ cym). Selected IR resonances (cm^{-1}, ATR): 2960, 1594, 1561, 1506, 1473, 1462, 1411, 1383, 1271, 1181, 1141, 1102, 809, 780, 743. Anal. Calcd for $C_{19}H_{19}IN_2O_3Ru$: C, 41.39; H, 3.47; N, 5.08. Found: C, 41.19; H, 3.33; N, 4.97. UV/vis (λ, nm (ε; L mol^{-1} cm^{-1})) c = 1 × 10^{-4} mol L^{-1}, $CHCl_3$: 373 (11300), 461 (22000). ESI-HRMS (CH_3CN) m/z (observed [M − I]$^+$, [M + H]$^+$ (expected)): 425.0440 (425.0439), 552.9564 (552.9562).

*$[Ru(\eta^6\text{-}p\text{-cxmene})N_3(nx)]$ (**1d**).* A 31.0 mg portion ofthe ruthenium azido precursor (**P4**, 0.0500 mmol), 19.0 mg of **nxH** (1.00 equiv, 0.10 mmol), and 5.4 mg of NaOMe (0.100 mmol) were suspended in 20 mL of acetone and stirred at room temperature for 3 h. The precipitate was filtered off, the orange filtrate was concentrated on a rotary evaporator, and the product was precipitated by the addition of

DOI: 10.1021/acs.inorgchem.9b01882
Inorg. Chem. 2019, 58, 12334−12347

n-hexane. The brown precipitate was collected by filtration and washed with *n*-hexane (η = 85%).

^{1}H NMR (400 MHz, $CDCl_3$): δ 9.59 (dd, J = 8.9, 1,3 Hz, 1H, C^2H), 8.99 (dd, J = 4.9, 1,3 Hz, 1H, C^4H), 8.60 (d, J = 9.3 Hz, 1H, C^6H), 7.70 (dd, J = 9.0, 4.9 Hz, 1H, C^3H), 6.93 (d, J = 9.3 Hz, 1H, C^7H), 5.67 (d, J = 6.0 Hz, 1H, Ar-*H* cym), 5.57 (d, J = 5.8 Hz, 1H, Ar-*H* cym), 5.47 (d, J = 6.0 Hz, 1H, Ar-*H* cym), 5.37 (d, J = 5.9 Hz, 1H, Ar-*H* cym), 2.81 (dt, J = 14,0, 7.0 Hz, 1H, Ar-C*H*$(CH_3)_2$ cym), 2.35 (s, 3H, Ar-CH_3 cym), 1,23 (d, J = 7.0 Hz, 6H, Ar-CH$(CH_3)_2$ cym). Selected IR resonances (cm^{-1}, ATR): 2961, 2027, 1595, 1565, 1507, 1475, 1465, 1415, 1274, 1181, 1146, 1104, 812, 793, 746. Anal. Calcd for $C_{19}H_{19}N_5O_3Ru$: C, 48.92; H, 4.11; N, 15.01. Found: C, 48.74; H, 4.03; N, 14.96. UV/vis (λ, nm (ε; L mol^{-1} cm^{-1})) $c = 1 \times 10^{-4}$ mol L^{-1}, $CHCl_3$: 273 (19400), 368 (8500), 469 (16400). ESI-HRMS (CH_3CN) m/z (observed $[M - N_3]^+$ (expected)): 425,0438 (425,0439).

[Ru(η^6-p-cymene)Cl($L^2H^{\pm}$)]PF_6 ***(2a)***. A 30.0 mg portion of the ruthenium chlorido precursor (**P1**, 0.0490 mmol), 32.5 mg of $\mathbf{L^2H}$ (1.00 equiv, 0.0980 mmol), and 20 mg of KPF_6 (1.10 equiv, 1.1 mmol) were dissolved in 20 mL of acetone, and the solution was stirred for 2 h at room temperature. KCl and excess KPF_6 were removed by filtration. The filtrate was concentrated on a rotary evaporator and precipitated by the addition of *n*-hexane. The orange precipitate was collected by filtration and washed with *n*-hexane (η = 85%).

^{1}H NMR (500 MHz, acetone-d_6): δ 9.42 (dd, J = 5.0, 1.3 Hz, 1H), 9.25 (dd, J = 8.9, 1.3 Hz, 1H), 8.56 (d, J = 18.4 Hz, 1H), 7.81 (dd, J = 8.9, 5.0 Hz, 1H), 5.88 (dd, J = 12.4, 6.2 Hz, 2H), 5.64 (dd, J = 5.9, 4.3 Hz, 2H), 4.84 (dd, J = 27.2, 13.3 Hz, 1H), 4.51 (t, J = 13.5 Hz, 1H), 3.72 (dd, J = 86.6, 12.9 Hz, 2H), 3.25 (t, J = 12.9 Hz, 2H), 2.81 (td, J = 8.6, 7.8, 6.0 Hz, 1H), 2.64 (tt, J = 12.1, 3.7 Hz, 1H), 2.17 (s, 3H), 1.96 (s, 2H), 1.22−1.09 (m, 7H). Selected IR resonances (cm^{-1}, ATR): 1716, 1597, 1562, 1518, 1466, 1410, 1287, 1197, 1136, 820. Anal. Calcd for $C_{26}H_{31}ClF_6N_3O_5PRu$: C, 41.86; H, 4.05; N, 5.63. Found: C, 41.70; H, 3.92; N, 5.42. UV/vis (λ, nm (ε; L mol^{-1} cm^{-1})) $c = 1 \times 10^{-4}$ mol L^{-1}, MeOH: 269 (11780), 346 (4700), 446 (9750). ESI-HRMS (CH_3CN) m/z (observed $[M - PF_6]^+$ (expected)): 602.0988 (602.0996).

[Ru(η^6-p-cymene)Br($L^2H^{\pm}$)]PF_6 ***(2b)***. A 39.5 mg portion of the ruthenium bromido precursor (**P2**, 0.049 mmol), 32.5 mg of $\mathbf{L^2H}$ (1.00 equiv, 0.098 mmol), and 20 mg of KPF_6 (1.10 equiv, 1.1 mmol) were dissolved in 20 mL of acetone, and the solution was stirred for 2 h at room temperature. KCl and excess KPF_6 were removed by filtration. The filtrate was concentrated on a rotary evaporator and precipitated by the addition of *n*-hexane. The reddish precipitate was collected by filtration and washed with *n*-hexane (η = 90%).

^{1}H NMR (500 MHz, acetone-d_6): δ 9.54 (dd, J = 5.1, 1.2 Hz, 1H), 9.38 (dd, J = 8.9, 1.2 Hz, 1H), 8.75 (d, J = 19.4 Hz, 1H), 7.95 (dd, J = 8.9, 5.0 Hz, 1H), 6.07−5.93 (m, 2H), 5.82 (t, J = 5.1 Hz, 2H), 4.91 (d, J = 13.7 Hz, 1H), 4.61 (d, J = 13.3 Hz, 1H), 3.90 (d, J = 12.8 Hz, 1H), 3.79 (d, J = 12.8 Hz, 1H), 3.45−3.27 (m, 2H), 3.02 (p, J = 6.9 Hz, 1H), 2.37 (s, 3H), 2.10 (s, 3H), 1.32−1.27 (m, 9H). Selected IR resonances (cm^{-1}, ATR):1718, 1592, 1560, 1517, 1465, 1390, 1279, 1195, 1158, 1134, 833, 750. Anal. Calcd for $C_{26}H_{31}BrF_6N_3O_5PRu$: C, 39.46; H, 3.91; N, 5.32. Found: C, 39.41; H, 4.19; N, 4.94. UV/vis (λ, nm (ε; L mol^{-1} cm^{-1})) $c = 1 \times 10^{-4}$ mol L^{-1}, MeOH: 259 (24800), 344 (9700), 429 (20000). ESI-HRMS (CH_3CN) m/z (observed $[M - PF_6]^+$ (expected)): 648.0475 (648.0470).

[Ru(η^6-p-cymene)Cl(L_3)] ***(3a)***. A 30.0 mg portion of the ruthenium chlorido precursor (**P1**, 0.049 mmol) and 29 mg of $\mathbf{L^3H}$ (1.00 equiv, 0.098 mmol) were dissolved in 20 mL of acetone, and the solution was stirred for 2 h at room temperature. The precipitated salt was removed by filtration. The filtrate was concentrated on a rotary evaporator and precipitated by the addition of *n*-hexane. The orange precipitate was collected by filtration and washed with *n*-hexane (η = 88%).

^{1}H NMR (500 MHz, chloroform-*d*): δ 12.78 (s, 1H), 9.49 (dd, J = 9.0, 1.2 Hz, 1H), 9.09 (dd, J = 5.0, 1.2 Hz, 1H), 8.64 (s, 1H), 7.71 (dd, J = 8.9, 4.9 Hz, 1H), 5.84−5.42 (m, 4H), 4.74 (d, J = 13.1 Hz, 1H), 4.23 (q, J = 13.2 Hz, 2H), 4.13−4.00 (m, 1H), 4.00−3.88 (m, 2H), 3.46 (d, J = 12.5 Hz, 1H), 3.32 (d, J = 12.0 Hz, 1H), 2.87 (td, J = 13.8, 7.1 Hz, 2H), 2.31 (s, 3H), 1.24 (dd, J = 10.9, 6.9 Hz, 6H). Selected IR resonances (cm^{-1}, ATR): 3455, 3057, 3027, 2970, 2464, 2431, 1738, 1587, 1558, 1515, 1491, 1467, 1449, 1403, 1377, 1277, 1231, 1217, 1189, 1130, 819. Anal. Calcd for $C_{24}H_{29}Cl_2N_3O_4Ru$: C, 48.49; H, 4.75; N, 7.07. Found: C, 48.19; H, 4.35; N, 7.07. UV/vis (λ, nm (ε; L mol^{-1} cm^{-1})) $c = 1 \times 10^{-4}$ mol L^{-1}, MeOH: 269 (12600), 344 (5000), 430 (11000). ESI-HRMS (CH_3CN) m/z (observed $[M - Cl]^+$ (expected)): 560.884 (560.0890).

[Ru(η^6-p-cymene)I(L^3)] ***(3c)***. A 31.0 mg portion of the ruthenium iodido precursor (**P3**, 0.030 mmol) and 18.5 mg of $\mathbf{L^3H}$ (1.00 equiv, 0.06 mmol) were dissolved in 20 mL of acetone, and the solution was stirred for 2 h at room temperature. The precipitated salt was removed by filtration. The filtrate was concentrated on a rotary evaporator and precipitated by the addition of *n*-hexane. The red precipitate was collected by filtration and washed with *n*-hexane (η = 82%).

^{1}H NMR (500 MHz, chloroform-*d*): δ 9.46 (dd, J = 8.9, 1.2 Hz, 1H), 9.04 (dd, J = 5.0, 1.2 Hz, 1H), 8.59 (s, 1H), 7.77−7.61 (m, 1H), 5.85 (dd, J = 11.6, 6.1 Hz, 2H), 5.75−5.59 (m, 2H), 5.03 (d, J = 13.4 Hz, 1H), 4.16 (s, 1H), 3.98 (t, J = 13.4 Hz, 3H), 3.78 (s, 1H), 3.51 (d, J = 12.4 Hz, 1H), 3.01 (p, J = 6.9 Hz, 2H), 2.40 (s, 3H), 1.28 (t, J = 6.9 Hz, 9H). Selected IR resonances (cm^{-1}, ATR): 2970, 1739, 1586, 1557, 1516, 1482, 1459, 1373, 1286, 1230, 1193, 1128, 1103, 911, 870, 822. Anal. Calcd for $C_{24}H_{29}I_2N_3O_4Ru$: C, 37.08; H, 3.63; N, 5.41. Found: C: 36.68; H, 3.33; N, 5.33. UV/vis (λ, nm (ε; L mol^{-1} cm^{-1})) $c = 1 \times 10^{-4}$ mol L^{-1}, MeOH: 260 (27000), 344 (11000), 439 (21500). ESI-HRMS (CH_3CN) m/z (observed $[M - I]^+$ (expected)): 652.0236 (652.0246).

[Ru(η^6-p-cymene)Cl(L^4)] ***(4a)***. A 30.0 mg portion of the ruthenium chlorido precursor (**P1**, 0.049 mmol) and 30 mg of $\mathbf{L^4H}$ (1.00 equiv, 0.098 mmol) were dissolved in 20 mL of acetone, and the solution was stirred for 2 h at room temperature. The precipitated salt was removed by filtration. The filtrate was concentrated on a rotary evaporator and precipitated by the addition of *n*-hexane. The orange precipitate was collected by filtration and washed with *n*-hexane. The crude product was purified by flash column chromatography on silica gel (η = 70%).

^{1}H NMR (500 MHz, chloroform-*d*): δ 9.56−9.39 (m, 1H), 8.96 (dd, J = 5.0, 1.3 Hz, 1H), 8.70 (s, 1H), 7.58 (dd, J = 8.9, 4.9 Hz, 1H), 5.67 (d, J = 6.0 Hz, 1H), 5.49 (dd, J = 21.3, 5.9 Hz, 2H), 5.39 (d, J = 5.8 Hz, 1H), 3.86 (d, J = 14.2 Hz, 1H), 3.60 (d, J = 14.2 Hz, 1H), 2.96−2.72 (m, 3H), 2.33 (s, 3H), 2.08 (dd, J = 13.0, 10.3 Hz, 2H), 1.59 (dt, J = 12.9, 3.1 Hz, 2H), 1.27 (d, J = 6.9 Hz, 4H), 1.17 (d, J = 6.9 Hz, 3H), 0.92 (d, J = 6.2 Hz, 3H). Selected IR resonances (cm^{-1}, ATR): 2951, 2923, 2871, 1793, 1589, 1557, 1515, 1455, 1376, 1268, 1230, 1217, 1192, 1156, 823. Anal. Calcd for $C_{26}H_{32}ClN_3O_3Ru$: C, 54.68; H, 5.65; N, 7.36. Found: C, 54.95; H, 5.29; N, 7.41. UV/vis (λ, nm (ε; L mol^{-1} cm^{-1})) $c = 1 \times 10^{-4}$ mol L^{-1}, MeOH: 271 (22200), 349 (8600), 456 (20400). ESI-HRMS (CH_3CN) m/z (observed $[M + H]^+$ (expected)): 572.1246 (572.1254).

[Ru(η^6-p-cymene)Cl(L^5)] ***(5a)***. A 30.0 mg portion of the ruthenium chlorido precursor (**P1**, 0.049 mmol) and 27 mg of $\mathbf{L^5H}$ (1.00 equiv, 0.098 mmol) were dissolved in 20 mL of acetone, and the solution was stirred for 2 h at room temperature. The precipitated salt was removed by filtration. The filtrate was concentrated on a rotary evaporator and precipitated by the addition of *n*-hexane. The brown precipitate was collected by filtration and washed with *n*-hexane. The crude product was purified by flash column chromatography on silica gel (η = 80%).

^{1}H NMR (500 MHz, acetone-d_6): δ 9.46 (dd, J = 5.0, 1.3 Hz, 1H), 9.33 (dd, J = 8.9, 1.2 Hz, 1H), 8.79 (s, 1H), 7.85 (dd, J = 8.9, 5.0 Hz, 1H), 5.97 (dd, J = 17.1, 5.9 Hz, 2H), 5.73 (dd, J = 16.4, 6.0 Hz, 2H), 4.22−4.05 (m, 2H), 3.52 (q, J = 7.0 Hz, 2H), 2.92 (hept, J = 7.0 Hz, 1H), 2.27 (s, 3H), 1.23−1.19 (m, 6H), 1.08 (t, J = 7.0 Hz, 3H). Selected IR resonances (cm^{-1}, ATR): 2970, 1587, 1557, 1513, 1448, 1376, 1260, 1233, 1187, 1128, 873, 819, 753, 673, 661. Anal. Calcd for $C_{23}H_{25}ClN_4O_3Ru$: C, 50.97; H, 4.65; N, 10.34. Found: C, 50.94; H, 4.65; N, 10.12. UV/vis (λ, nm (ε; L mol^{-1} cm^{-1})) $c = 1 \times 10^{-4}$

DOI: 10.1021/acs.inorgchem.9b01882
Inorg. Chem. 2019, 58, 12334−12347

mol L^{-1}, MeOH: 271 (15000), 350 (5700), 456 (13000). ESI-HRMS (CH_3CN) m/z observed $[M + H]^+$ expected)): 543.0730 (543.0737).

*[Ru(η^6-p-cymene)Cl($L^6H^{\pm}$)]PF_6 (**6a**).* A 30.0 mg portion of the ruthenium chlorido precursor (**P1**, 0.049 mmol), 28 mg of L^6H (1.00 equiv, 0.098 mmol), and 20 mg of KPF_6 (1.10 equiv, 1.1 mmol) were dissolved in 20 mL of acetone, and the solution was stirred for 2 h at room temperature. KCl and excess KPF_6 were removed by filtration. The filtrate was concentrated on a rotary evaporator and precipitated by the addition of *n*-hexane. The orange precipitate was collected by filtration and washed with *n*-hexane (η = 90%).

^{1}H NMR (500 MHz, acetone-d_6): δ 9.55 (dd, J = 5.0, 1.2 Hz, 1H), 9.40 (dd, J = 9.0, 1.1 Hz, 1H), 8.71 (s, 1H), 7.95 (ddd, J = 9.0, 4.9, 0.9 Hz, 1H), 6.04−5.98 (m, 2H), 5.78 (t, J = 6.3 Hz, 2H), 5.05−4.97 (m, 1H), 4.66−4.59 (m, 1H), 3.89−3.81 (m, 1H), 3.80−3.72 (m, 1H), 3.56 (d, J = 10.7 Hz, 1H), 3.45 (dq, J = 13.6, 7.6, 6.8 Hz, 1H), 2.95 (dt, J = 14.5, 7.3 Hz, 1H), 2.32 (s, 3H), 2.10 (d, J = 1.2 Hz, 3H), 1.36−1.23 (m, 7H). Selected IR resonances (cm^{-1}, ATR): 2971, 1739, 1592, 1562, 1519, 1464, 1366, 1286, 1217, 1135, 815, 751. Anal. Calcd for $C_{24}H_{28}ClF_6N_3O_5PRu$: C, 41.90; H, 4.10; N, 6.11. Found: C, 41.52; H, 3.92; N, 5.94. UV/vis (λ, nm (ε; L mol^{-1} cm^{-1})) $c = 1 \times 10^{-4}$ mol L^{-1}, MeOH: 269 (10000), 344 (4170), 444 (9200). ESI-HRMS (CH_3CN) m/z (observed $[M - PF_6]^+$ (expected)): 544.0937 (544.0900).

Enzyme Kinetics. Human recombinant catB was prepared as reported.[65] For the catB endopeptidase and exopeptidase assay 100 mM phosphate buffer (pH 6.0) and 60 mM acetate buffer (pH 5.0) were respectively used. Each contained 0.1% PEG 8000 (Sigma-Aldrich, St. Louis, MO, USA), 5 mM cysteine, and 1.5 mM EDTA. Prior to the assay, the enzyme was activated in the assay buffer for 5 min at 37 °C.

Determination of Relative Inhibition. The effect of inhibitors on catB endopeptidase and exopeptidase activity was determined using the substrates Z-Arg-Arg-AMC and Abz-Gly-Ile-Val-Arg-Ala-Lys-(Dnp)-OH (Bachem, Bubendorf, Switzerland), respectively. The reaction was initiated by adding 90 μL of activated enzyme in the assay buffer to the wells of a black microplate containing 5 μL of substrate at final concentrations of 5 and 1 μM for endopeptidase and exopeptidase activity, respectively, and 5 μL of inhibitor at a concentration of 50 μM. The formation of the fluorescent degradation products during the reaction was continuously monitored at 460 ± 10 nm with excitation at 380 ± 20 and at 420 ± 10 nm with excitation at 320 ± 20 nm for Z-Arg-Arg-AMC and Abz-Gly-Ile-Val-Arg-Ala-Lys(Dnp)-OH, respectively, at 37 °C on a Tecan Safire^2 apparatus (Mannedorf, Switzerland). All assay mixtures contained 5% (v/v) DMSO. To prevent false-positive inhibition due to the formation of compound aggregates, 0.01% Triton X-100 was used.[66] All measurements were performed in triplicate and repeated twice. The relative inhibition was calculated using the following equation: relative inhibition (%) = $100(1 - v_i/v_o)$, where v_i and v_o designate the reaction velocities in the presence and absence of inhibitor, respectively.

Determination of K_i Values. Inhibition constants were calculated from the reaction velocities measured at three substrate concentrations in the presence of seven concentrations of inhibitor (0, 20, 40, 60, 80, 100, and 200 μM). The reaction was initiated by adding 90 μL of enzyme in the assay buffer to the wells of a black microplate with 5 μL of substrate and 5 μL of inhibitor. To assess cathepsin B endopeptidase and exopeptidase activity, the substrate Z-Arg-Arg-AMC at concentrations of 60, 180, and 360 μM and the substrate Abz-Gly-Ile-Val-Arg-Ala-Lys(Dnp)-OH at concentrations of 1, 3, and 6 μM were used, respectively. Formation of the fluorescent degradation products was monitored as described above. All assay mixtures contained 5% (v/v) DMSO. All measurements were performed in duplicate and repeated three times. The SigmaPlot12, Enzyme Kinetics Module 1.3 was used for calculation of K_i values.

Microscale Thermophoresis. The binding affinity of ruthenium complexes with catB was evaluated using microscale thermophoresis (MST) on a Monolith NT.115pico Red apparatus (Nanotemper Technologies, Munich, Germany). MST is a biophysical method that allows quantitative analysis of wide range of bimolecular interactions in free solution. It is based on the change in motion of fluorescently labeled molecules in a temperature gradient following the ligand binding.[49,50]

For MST detection, recombinant catB was fluorescently labeled using Monolith NT Protein Labeling Kit RED-NHS (Nanotemper Technologies) with the red fluorescent dye NT-647-NHS (Nanotemper Technologies) according to the manufacturer's instructions. Sixteen-step serial dilutions of inhibitors were prepared in 100 mM phosphate buffer (pH 6.0) supplemented with 0.1% PEG 8000, 5 mM cysteine, 1.5 mM EDTA, and 0.05% Tween 20 starting with the final concentration of 1000 μM for each compound. The labeled catB was diluted in assay buffer to a final assay concentration of 5 nM, activated for 5 min at 37 °C prior to the assay, and added to the serial dilutions of inhibitors in a 1:1 volumetric ratio. All assay mixtures contained 5% (v/v) DMSO. The samples were loaded into Monolith NT.115 Standard Treated Capillaries (Nanotemper Technologies). The experiments were performed using medium MST power (40%) and 60% excitation power. Measurements were repeated at least twice. Binding affinities expressed as constants of dissociation (K_d) were obtained by fitting normalized fluorescence (F_{norm}) calculated from MST traces as the ratio between fluorescence after thermodiffusion and the initial fluorescence against increasing inhibitor concentrations. Data were analyzed using MO Affinity Analysis Software (Nanotemper Technologies).

Cell Culture. MCF-10A neoT, a c-Ha-ras oncogene transfected human breast epithelial cell line, was provided by Bonnie F. Sloane (Wayne State University, Detroit, MI). MCF-10A neoT cells were cultured in DMEM/F12 (1/1) medium (Gibco, Carlsbad, CA, USA) supplemented with 5% fetal bovine serum (FBS, Gibco), 1 μg/mL of insulin (Sigma-Aldrich), 0.5 μg/mL of hydrocortisone (Sigma-Aldrich), 20 ng/mL of EGF (Sigma-Aldrich), 2 mM glutamine (Gibco), and antibiotics at 37 °C in a humidified atmosphere containing 5% CO_2 until being 80% confluent. Prior to use, cells were detached from the culture flask using 0.05% trypsin (Gibco) and 0.02% EDTA in phosphate buffered saline (PBS), pH 7.4.

Cell Viability Assay. The effect of ruthenium complexes with nitroxoline and its derivatives on the cell viability of the MCF-10A neoT cells was assessed using an MTS (3-(4,5-dimethylthiazol-2-yl)-5-(3-carboxymethoxyphenyl)-2-(4-sulfophenyl)-2*H*-tetrazolium) colorimetric assay. Into wells of a 96-well microplate were seeded 1×10^4 cells and incubated overnight to attach. The medium was replaced with 200 μL of medium containing 0.25, 0.5, 1.25, 2.5, or 5 μM of the respective compound or DMSO (0.05%). After 72 h treatment, 10 μL of MTS (Promega, Madison, WI, USA) was added to the wells and the following incubation absorbance of formazan was measured at 492 nm on a Tecan Safire^2 apparatus. The cell viability (%) was expressed as the ratio between absorbance obtained in the presence of compounds versus DMSO. All assays were performed in quadruplicate and repeated at least two times.

DQ-Collagen IV Degradation Assay. The effect of ruthenium complexes with nitroxoline and its derivatives on degradation of the extracellular matrix (ECM) was measured by monitoring the degradation of DQ-collagen IV. Flow cytometry was used to evaluate the intracellular degradation of DQ-collagen IV by MCF-10A neoT cells. Into the wells of a 24-well plate 6×10^4 MCF-10A neoT cells were seeded and incubated overnight to attach. Cells were then treated with the respective compound (1.25 μM and 0.5 μM for **1c**) or DMSO (0.5%) in 500 μL of serum-free medium (SFM) for 2 h at 37 °C. Afterward, DQ-collagen IV (5 μg/mL; Thermo Fischer, Rockford, IL, USA) was added and cells were incubated for an additional 2 h at 37 °C. Propidium iodide (BD Biosciences) was used to exclude dead cells, and green fluorescence arising from DQ-collagen IV degradation was monitored only for viable cells. Samples were measured on a FACSCalibur instrument (BD Biosciences).

To monitor the extracellular degradation of DQ-collagen IV, spectrofluorimetry was used. Into wells of a 96-well microplate were plated 5×10^4 MCF-10A neoT cells and incubated overnight to attach. Cells were then treated with compounds (1.25 and 0.5 μM for **1c**) or DMSO (0.05%) and DQ-collagen IV (10 μg/mL) in 100 μL of PBS for 6 h at 37 °C. Following treatment, the reaction mixture (80

DOI: 10.1021/acs.inorgchem.9b01882
Inorg. Chem. 2019, 58, 12334−12347

μL) was transferred into empty wells of a 96-well black microplate, where the fluorescence intensity was continuously monitored for 2 h at 515 ± 5 nm with excitation at 495 ± 5 nm on a Tecan Safire^2 apparatus. The inhibition of extracellular DQ-collagen IV degradation was expressed as the ratio between the average 2 h fluorescence obtained in the presence of compounds versus DMSO.

Real-Time Invasion Assay. A real-time tumor cell invasion assay to monitor the effect of ruthenium complexes with nitroxoline and its derivatives on MCF-10A neoT cells was performed on the xCELLigence Real Time Cell Analyzer (RTCA; ACEA Biosciences Inc., San Diego, CA, USA). Prior to the assay, the cells were serum starved for 24 h. First, on the CIM-plate 16 (ACEA Biosciences Inc.) the down sides of the microporous PET membrane were coated with 0.3 μg of fibronectin from bovine plasma (Calbiochem, Darmstadt, Germany) for 30 min at room temperature. Then, the upper chambers of CIM-plate 16 wells were coated with 20 μL of Matrigel (1 mg/mL; BD Biosciences, Franklin Lakes, NJ, USA) in serum-free medium (SFM) and allowed to gel for 30 min at 37 °C. The compound (1.25 or 0.5 μM for compound **1c**) in the complete medium (180 μL) was added to the lower chambers and afterward the top and bottom parts of the CIM-plate 16 were assembled together. To the upper chambers was added the compound (1.25 or 0.5 μM for compound **1c**) in 60 μL of SFM. DMSO (0.05%) was used as a control. The CIM-plate 16 was allowed to equilibrate for 1 h at 37 °C. Finally, after equilibration, MCF-10A neoT cells (3×10^4 cells/well) in 80 μL of SFM were seeded in the top chambers of CIM-plate 16. The xCELLigence system measured impedance data, reported as cell index (CI), in real time every 15 min during the entire course of the experiment for 72 h. Obtained data were analyzed using the RTCA Software (Roche). The relative invasion (%) was expressed as a percentage relative to the control cells treated with DMSO.

Statistical Analysis. Data were analyzed using the GraphPad Prism 6.0 software package and are presented as mean ± SEM unless stated otherwise. Results were compared by Student's t test (nonparametric, two-tailed). Differences were considered significant at $P \leq 0.05$.

■ ASSOCIATED CONTENT

Supporting Information

The Supporting Information is available free of charge on the ACS Publications website at DOI: 10.1021/acs.inorgchem.9b01882.

Crystallographic data table and NMR solution stability studies of compound **1a** in DMSO-d_6 and D_2O (PDF)

Accession Codes

CCDC 1909464−1909466 contain the supplementary crystallographic data for this paper. These data can be obtained free of charge via www.ccdc.cam.ac.uk/data_request/cif, or by emailing data_request@ccdc.cam.ac.uk, or by contacting The Cambridge Crystallographic Data Centre, 12 Union Road, Cambridge CB2 1EZ, UK; fax: +44 1223 336033.

■ AUTHOR INFORMATION

Corresponding Authors

*E-mail for J.K.: janko.kos@ffa.uni-lj.si.
*E-mail for I.T.: iztok.turel@fkkt.uni-lj.si.

ORCID

Izidor Sosič: 0000-0002-3370-4587
Stanislav Gobec: 0000-0002-9678-3083
Iztok Turel: 0000-0001-6776-4062

Author Contributions

‖A.M. and J.K. contributed equally.

Notes

The authors declare no competing financial interest.

■ ACKNOWLEDGMENTS

The authors wish to thank the Slovenian Research Agency for financial support (Z1-6735, P1-0175, Junior Researcher Grant for M.U., P4-0127, P1-0208, J4-8227 and Z3-9273). The EN → FIST Centre of Excellence, Trg OF 13, SI-1000 Ljubljana, Slovenia, is acknowledged for the use of the SuperNova diffractometer.

■ REFERENCES

(1) Mohamed, M. M.; Sloane, B. F. Cysteine cathepsins: multifunctional enzymes in cancer. *Nat. Rev. Cancer* **2006**, *6*, 764−775.

(2) Kos, J.; Mitrović, A.; Mirković, B. The current stage of cathepsin B inhibitors as potential anticancer agents. *Future Med. Chem.* **2014**, *6*, 1355−1371.

(3) Vasiljeva, O.; Reinhackel, T.; Peters, C.; Turk, D.; Turk, V.; Turk, B. Emerging roles of cysteine cathepsins in disease and their potential as drug targets. *Curr. Pharm. Des.* **2007**, *13*, 387−403.

(4) Joyce, J. A.; Hanahan, D. Multiple roles for cysteine cathepsins in cancer. *Cell Cycle* **2004**, *3*, 1516−1519.

(5) Musil, D.; Zucic, D.; Turk, D.; Engh, R. A.; Mayr, I.; Huber, R.; Popovic, T.; Turk, V.; Towatari, T.; Katunuma, N.; Bode, W. The refined 2.15 A X-ray crystal structure of human liver cathepsin B: the structural basis for its specificity. *EMBO J.* **1991**, *10*, 2321−2330.

(6) Nägler, D. K.; Storer, A. C.; Portaro, F. C. V.; Carmona, E.; Juliano, L.; Ménard, R. Major Increase in Endopeptidase Activity of Human Cathepsin B upon Removal of Occluding Loop Contacts. *Biochemistry* **1997**, *36*, 12608−12615.

(7) Illy, C.; Quraishi, O.; Wang, J.; Purisima, E.; Vernet, T.; Mort, J. S. Role of the Occluding Loop in Cathepsin B Activity. *J. Biol. Chem.* **1997**, *272*, 1197−1202.

(8) Krupa, J. C.; Hasnain, S.; Nägler, D. K.; Ménard, R.; Mort, J. S. S2′ substrate specificity and the role of His110 and His111 in the exopeptidase activity of human cathepsin B. *Biochem. J.* **2002**, *361*, 613−619.

(9) Almeida, P. C.; Nantes, I. L.; Chagas, J. R.; Rizzi, C. C.; Faljoni-Alario, A.; Carmona, E.; Juliano, L.; Nader, H. B.; Tersariol, I. L. Cathepsin B activity regulation. Heparin-like glycosaminogylcans protect human cathepsin B from alkaline pH-induced inactivation. *J. Biol. Chem.* **2001**, *276*, 944−951.

(10) Roshy, S.; Sloane, B. F.; Moin, K. Pericellular cathepsin B and malignant progression. *Cancer Metastasis Rev.* **2003**, *22*, 271−286.

(11) Mitrović, A.; Mirkovic, B.; Sosič, I.; Gobec, S.; Kos, J. Inhibition of endopeptidase and exopeptidase activity of cathepsin B impairs extracellular matrix degradation and tumour invasion. *Biol. Chem.* **2016**, *397*, 165−174.

(12) Gocheva, V.; Zeng, W.; Ke, D. X.; Klimstra, D.; Reinheckel, T.; Peters, C.; Hanahan, D.; Joyce, J. A. Distinct roles for cysteine cathepsin genes in multistage tumorigenesis. *Genes Dev.* **2006**, *20*, 543−556.

(13) Vasiljeva, O.; Korovin, M.; Gajda, M.; Brodoefel, H.; Bojic, L.; Kruger, A.; Schurigt, U.; Sevenich, L.; Turek, B.; Peters, C.; Reinheckel, T. Reduced tumour cell proliferation and delayed development of high-grade mammary carcinomas in cathepsin B-deficient mice. *Oncogene* **2008**, *27*, 4191−4199.

(14) Gopinathan, A.; Denicola, G. M.; Frese, K. K.; Cook, N.; Karreth, F. A.; Mayerle, J.; Lerch, M. M.; Reinheckel, T.; Tuveson, D. A. Cathepsin B promotes the progression of pancreatic ductal adenocarcinoma in mice. *Gut* **2012**, *61*, 877−884.

(15) Mirkovic, B.; Renko, M.; Turk, S.; Sosic, I.; Jevnikar, Z.; Obermajer, N.; Turk, D.; Gobec, S.; Kos, J. Novel Mechanism of Cathepsin B Inhibition by Antibiotic Nitroxoline and Related Compounds. *ChemMedChem* **2011**, *6*, 1351−1356.

(16) Schmitz, J.; Gilbert, E.; Löser, R.; Bajorath, J.; Bartz, U.; Gütschow, M. Cathepsin B: Active site mapping with peptidic substrates and inhibitors. *Bioorg. Med. Chem.* **2019**, *27*, 1−15.

(17) Mirković, B.; Markelc, B.; Butinar, M.; Mitrović, A.; Sosič, I.; Gobec, S.; Vasiljeva, O.; Turk, B.; Čemežar, M.; Serša, G.; Kos, J.

DOI: 10.1021/acs.inorgchem.9b01882
Inorg. Chem. 2019, 58, 12334−12347

Nitroxoline impairs tumor progression *in vitro* and *in vivo* by regulating cathepsin B activity. *Oncotarget* **2015**, *6*, 19027−19042.
(18) Sosic, I.; Mirkovic, B.; Arenz, K.; Stefane, B.; Kos, J.; Gobec, S. Development of New Cathepsin B Inhibitors: Combining Bioisosteric Replacements and Structure-Based Design To Explore the Structure-Activity Relationships of Nitroxoline Derivatives. *J. Med. Chem.* **2013**, *56*, 521−533.
(19) Sosič, I.; Mitrović, A.; čurić, H.; Knez, D.; Brodnik Žugelj, H.; Štefane, B.; Kos, J.; Gobec, S. Cathepsin B inhibitors: Further exploration of the nitroxoline core. *Bioorg. Med. Chem. Lett.* **2018**, *28*, 1239−1247.
(20) Mitrović, A.; Sosič, I.; Kos, Š.; Lampreht Tratar, U.; Breznik, B.; Kranjc, S.; Mirković, B.; Gobec, S.; Lah, T.; Čemažar, M.; Serša, G.; Kos, J. Addition of 2-(ethylamino)acetonitrile group to nitroxoline results in significantly improved anti-tumor activity in vitro and in vivo. *Oncotarget* **2017**, *8*, 59136−59147.
(21) Alessio, E. *Bioinorganic Medicinal Chemistry*; Wiley-VCH: Weinheim, Germany, 2011.
(22) Chitambar, C. R. Gallium-containing anticancer compounds. *Future Med. Chem.* **2012**, *4*, 1257−1272.
(23) Tabti, R.; Tounsi, N.; Gaiddon, C.; Bentouhami, E.; Désaubry, L. Progress in copper complexes as anticancer agents. *Med. Chem.* **2017**, *07*, 875−879.
(24) Schilling, T.; Keppler, B. K.; Heim, M. E.; Niebch, G.; Dietzfelbinger, H.; Rastetter, J.; Hanauske, A.-R. Clinical phase I and pharmacokinetic trial of the new titanium complex budotitane. *Invest. New Drugs* **1995**, *13*, 327−332.
(25) Trondl, L.; Heffeter, P.; Kowol, C. R.; Jakupec, M. A.; Berger, W.; Keppler, B. K. NKP-1339, the first ruthenium-based anticancer drug on the edge to clinical application. *Chem. Sci.* **2014**, *5*, 2925−2932.
(26) Leijen, S.; Burgers, S. A.; Baas, P.; Pluim, D.; Tibben, M.; van Werkhoven, E.; Alessio, E.; Sava, G.; Beijnen, J. H.; Schellens, J. H. M. Phase I/II study with ruthenium compound NAMI-A and gemcitabine in patients with non-small cell lung cancer after first line therapy. *Invest. New Drugs* **2015**, *33*, 201−214.
(27) Heinemann, F.; Karges, J.; Gasser, G. Critical overview of the use of Ru(II) polypyridyl complexes as photosensitizers in one-photon and two-photon photodynamic therapy. *Acc. Chem. Res.* **2017**, *50*, 2727−2736.
(28) Gobec, M.; Kljun, J.; Sosič, I.; Mlinarič-Raščan, I.; Uršič, M.; Gobec, S.; Turel, I. Structural characterization and biological evaluation of a clioquinol-ruthenium complex with copper-independent antileukaemic activity. *Dalton Trans* **2014**, *43*, 9045−9051.
(29) Mitrović, A.; Kljun, J.; Sosič, I.; Gobec, S.; Turel, I.; Kos, J. Clioquinol-ruthenium complex impairs tumour cell invasion by inhibiting cathepsin B activity. *Dalton Trans* **2016**, *45*, 16913−16921.
(30) Živković, M. D.; Kljun, J.; Ilić-Tomić, T.; Pavić, A.; Veselinović, A.; Manojlović, D. D.; Nikodinović-Runić, J.; Turel, I. A new class of platinum(II) complexes with phosphine ligand pta which show potent anticancer activity. *Inorg. Chem. Front.* **2018**, *5*, 39−53.
(31) Kljun, J.; León, I. E.; Peršič, Š.; Cadavid-Vargas, J. F.; Etcheverry, S.; He, W.; Bai, Y.; Turel, T. Synthesis and characterization of organoruthenium complexes with 8-hydroxyquinolines. *J. Inorg. Biochem.* **2018**, *186*, 187−196.
(32) Ruiz, M. C.; Kljun, J.; Turel, I.; Di Virgilio, A. L.; León, I. E. Comparative antitumor studies of organoruthenium complexes with 8-hydroxyquinolines on 2D and 3D cell models of bone, lung and breast cancer. *Metallomics* **2019**, *11*, 666−675.
(33) Uzelac, M.; Ristovski, S.; Sepčić, K.; Kljun, J.; Lipec, T.; Uršič, M.; Turel, I.; Zemljič Jokhadar, Š.; Žužek, M.; Trobec, T.; Frangež, R. Organoruthenium prodrugs as a new class of cholinesterase and glutathione-S-transferase inhibitors. *ChemMedChem* **2018**, *13*, 2166−2176.
(34) Sheng, Y.; Hou, Z.; Cui, S.; Cao, K.; Sun, M.; Kljun, J.; Huang, G.; Turel, I.; Liu, Y. Covalent versus Non covalent Binding of Ruthenium η^6 *p* Cymene Complexes to Zinc finger Protein NCp7. *Chem. - Eur. J.* **2019**, DOI: 10.1002/chem.201902434.
(35) Zhu, Y. B.; Cameron, B. R.; Mosi, R.; Anastassov, V.; Cox, J.; Qin, L.; Santucci, Z.; Metz, M.; Skerlj, R. T.; Fricker, S. P. Inhibition of the cathepsin cysteine proteases B and K by square-planar cycloaurated gold(III) compounds and investigation of their anticancer activity. *J. Inorg. Biochem.* **2011**, *105*, 754−762.
(36) Mosi, R.; Baird, I. R.; Cox, J.; Anastassov, V.; Cameron, B.; Skerlj, R. T.; Fricker, S. P. Rhenium inhibitors of cathepsin B (ReO(SYS)X (Where Y = S, py; X = Cl, Br, SPhOMe-p)): Synthesis and mechanism of inhibition. *J. Med. Chem.* **2006**, *49*, 5262−5272.
(37) Casini, A.; Gabbiani, C.; Sorrentino, F.; Rigobello, M. P.; Bindoli, A.; Geldbach, T. J.; Marrone, A.; Re, N.; Hartinger, C. G.; Dyson, P. J.; Messori, L. Emerging Protein Targets for Anticancer Metallodrugs: Inhibition of Thioredoxin Reductase and Cathepsin B by Antitumor Ruthenium (II)-Arene Compounds. *J. Med. Chem.* **2008**, *51*, 6773−6781.
(38) Kljun, J.; Bratsos, I.; Alessio, E.; Psomas, G.; Repnik, U.; Butinar, M.; Turk, B.; Turel, I. New Uses for Old Drugs: Attempts to Convert Quinolone Antibacterials into Potential Anticancer Agents Containing Ruthenium. *Inorg. Chem.* **2013**, *52*, 9039−9052.
(39) Hudej, R.; Kljun, J.; Kandioller, W.; Repnik, U.; Turk, B.; Hartinger, C. G.; Keppler, B. K.; Miklavcic, D.; Turel, I. Synthesis and Biological Evaluation of the Thionated Antibacterial Agent Nalidixic Acid and Its Organoruthenium(II) Complex. *Organometallics* **2012**, *31*, 5867−5874.
(40) Li, J.; Tian, Z.; Ge, X.; Xu, Z.; Feng, Y.; Liu, Z. Design, synthesis, and evaluation of fluorine and Naphthyridine−Based half-sandwich organoiridium/ruthenium complexes with bioimaging and anticancer activity. *Eur. J. Med. Chem.* **2019**, *163*, 830−839.
(41) Respondek, T.; Garner, R. N.; Herroon, M. K.; Podgorski, I.; Turro, C.; Kodanko, J. J. Light Activation of a Cysteine Protease Inhibitor: Caging of a Peptidomimetic Nitrile with $Ru^{II}(bpy)_2$. *J. Am. Chem. Soc.* **2011**, *133*, 17164−17167.
(42) Respondek, T.; Sherma, R.; Herroon, M. K.; Garner, R. N.; Knoll, J. D.; Cueny, E.; Turro, C.; Podgorski, I.; Kodanko, J. J. Inhibition of Cathepsin Activity in a Cell-Based Assay by a Light-Activated Ruthenium Compound. *ChemMedChem* **2014**, *9*, 1306−1315.
(43) Arora, K.; Herroon, M.; Al-Afyouni, M. H.; Toupin, N. P.; Rohrabaugh, T. N.; Loftus, L. M.; Podgorski, I.; Turro, C.; Kodanko, J. J. Catch and Release Photosensitizers: Combining Dual-Action Ruthenium Complexes with Protease Inactivation for Targeting Invasive Cancers. *J. Am. Chem. Soc.* **2018**, *140*, 14367−14380.
(44) Thai, T. T.; Therrien, B.; Suss-Fink, G. Arene ruthenium oxinato complexes: Synthesis, molecular structure and catalytic activity for the hydrogenation of carbon dioxide in aqueous solution. *J. Organomet. Chem.* **2009**, *694*, 3973−3981.
(45) Kubanik, M.; Holtkamp, H.; Söhnel, T.; Jamieson, S. M. F.; Hartinger, C. G. Impact of the Halogen Substitution Pattern on the Biological Activity of Organoruthenium 8-Hydroxyquinoline Anticancer Agents. *Organometallics* **2015**, *34*, 5658−5668.
(46) Movassaghi, S.; Hanif, M.; Holtkamp, H. U.; Söhnel, T.; Jamieson, S. M. F.; Hartinger, C. G. Making organoruthenium complexes of 8-hydroxyquinolines more hydrophilic: impact of a novel L-phenylalanine-derived arene ligand on the biological activity. *Dalton Trans* **2018**, *47*, 2192−2201.
(47) Schuecker, R.; John, R. O.; Jakupec, M. A.; Arion, V. B.; Keppler, B. K. Water-Soluble Mixed-Ligand Ruthenium(II) and Osmium(II) Arene Complexes with High Antiproliferative Activity. *Organometallics* **2008**, *27*, 6587−6595.
(48) Wang, F. Y.; Habtemariam, A.; van der Geer, E. P. L.; Fernandez, R.; Melchart, M.; Deeth, R. J.; Aird, R.; Guichard, S.; Fabbiani, F. P. A.; Lozano-Casal, P.; Oswald, I. D. H.; Jodrell, D. I.; Parsons, S.; Sadler, P. J. Controlling ligand substitution reactions of organometallic complexes: Tuning cancer cell cytotoxicity. *Proc. Natl. Acad. Sci. U. S. A.* **2005**, *102*, 18269−18274.
(49) Seidel, S. A.; Dijkman, P. M.; Lea, W. A.; van den Bogaart, G.; Jerabek-Willemsen, M.; Lazic, A.; Joseph, J. S.; Srinivasan, P.; Baaske, P.; Simeonov, A.; Katritch, I.; Melo, F. A.; Ladbury, J. E.; Schreiber, G.; Watts, A.; Braun, S.; Duhr, S. Microscale thermophoresis

DOI: 10.1021/acs.inorgchem.9b01882
Inorg. Chem. 2019, 58, 12334−12347

quantifies biomolecular interactions under previously challenging conditions. *Methods* **2013**, *59*, 301−315.
(50) Jerabek-Willemsen, M.; Wienken, C. J.; Braun, D.; Baaske, P.; Duhr, S. Molecular Interaction Studies Using Microscale Thermophoresis. *Assay Drug Dev. Technol.* **2011**, *9*, 342−353.
(51) Zaltariov, M. F.; Hammerstad, M.; Arabshahi, H. J.; Jovanović, K.; Richter, K. W.; Cazacu, M.; Shova, S.; Balan, M.; Andersen, N. H.; Radulović, S.; Reynisson, J.; Andersson, K. K.; B, A. V. New Iminodiacetate-Thiosemicarbazone Hybrids and Their Copper(II) Complexes Are Potential Ribonucleotide Reductase R2 Inhibitors with High Antiproliferative Activity. *Inorg. Chem.* **2017**, *56*, 3532−3549.
(52) Premzl, A.; Zavašnik-Bergant, V.; Turk, V.; Kos, J. Intracellular and extracellular cathepsin B facilitate invasion of MCF-10A neoT cells through reconstituted extracellular matrix in vitro. *Exp. Cell Res.* **2003**, *283*, 206−214.
(53) Sevenich, L.; Schurigt, U.; Sachse, K.; Gajda, M.; Werner, F.; Muller, S.; Vasiljeva, O.; Schwinde, A.; Klemm, N.; Deussing, J.; Peters, C.; Reinheckel, T. Synergistic antitumor effects of combined cathepsin B and cathepsin Z deficiencies on breast cancer progression and metastasis in mice. *Proc. Natl. Acad. Sci. U. S. A.* **2010**, *107*, 2497−2502.
(54) Vasiljeva, O.; Papazoglou, A.; Kruger, A.; Brodoefel, H.; Korovin, M.; Deussing, J.; Augustin, N.; Nielsen, B. S.; Almholt, K.; Bogyo, M.; Peters, C.; Reinheckel, T. Tumor Cell−Derived and Macrophage-Derived Cathepsin B Promotes Progression and Lung Metastasis of Mammary Cancer. *Cancer Res.* **2006**, *66*, 5242−5250.
(55) Shim, J. S.; Matsui, Y.; Bhat, S.; Nacev, B. A.; Xu, J.; Bhang, H. E.; Dhara, S.; Han, K. C.; Chong, C. R.; Pomper, M. G.; So, A.; Liu, J. O. Effect of nitroxoline on angiogenesis and growth of human bladder cancer. *J. Natl. Cancer Inst.* **2010**, *102*, 1855−1873.
(56) Prachayasittikul, V.; Chan-On, W.; Nguyen Thi Bich, H.; Songtawee, N.; Suwanjang, W.; Prachayasittikul, S. Quinoline-based clioquinol and nitroxoline exhibit anticancer activity inducing FoxM1 inhibition in cholangiocarcinoma cells. *Drug Des., Dev. Ther.* **2015**, *9*, 2033−2047.
(57) Jiang, H.; Xing, J.; Wang, C.; Zhang, H.; Yue, L.; Wan, X.; Chen, W.; Ding, H.; Xie, Y.; Tao, H.; Chen, Z.; Jiang, H.; Chen, K.; Chen, S.; Zheng, M.; Zhang, Y.; Luo, C. Discovery of novel BET inhibitors by drug repurposing of nitroxoline and its analogues. *Org. Biomol. Chem.* **2017**, *15*, 9352−9361.
(58) Lazovic, J.; Guo, L.; Nakashima, J.; Mirsaraei, L.; Yong, W.; Kim, H. J.; Ellingson, B.; Wu, H.; Pope, W. B. Nitroxoline induces apoptosis and slows glioma growth in vivo. *Neuro. Oncol.* **2015**, *17*, 53−62.
(59) Chang, W. L.; Hsu, L. C.; Leu, W. J.; Chen, C. S.; Guh, J. H. Repurposing of nitroxoline as a potential anticancer agent against human prostate cancer: a crucial role on AMPK/mTOR signaling pathway and the interplay with Chk2 activation. *Oncotarget* **2015**, *6*, 39806−39820.
(60) Mao, H.; Du, Y.; Zhang, Z.; Cao, B.; Zhao, J.; Zhou, H.; Mao, X. Nitroxoline shows antimyeloma activity by targeting the TRIM25/p53 axle. *Anti-Cancer Drugs* **2017**, *28*, 376−383.
(61) Mendoza-Ferri, M. G.; Hartinger, C. G.; Nazarov, A. A.; Eichinger, R. E.; Jakupec, M. A.; Severin, K.; Keppler, B. K. Influence of the arene ligand, the number and type of metal centers, and the leaving group on the in vitro antitumor activity of polynuclear organometallic compounds. *Organometallics* **2009**, *28*, 6260−6265.
(62) Lalrempuia, R.; Yennawar, H. P.; Kollipara, M. R. Mono- and di-nuclear azido η^6-*p*-cymene ruthenium(II) complexes; synthesis, reactivity, and structures. *J. Coord. Chem.* **2009**, *62*, 3661−3678.
(63) Dolomanov, O. V.; Bourhis, L. J.; Gildea, R. J.; Howard, J. A. K.; Puschmann, H. OLEX2: a complete structure solution, refinement and analysis program. *J. Appl. Crystallogr.* **2009**, *42*, 339−341.
(64) Sheldrick, G. SHELXT - Integrated space-group and crystal-structure determination. *Acta Crystallogr., Sect. A: Found. Adv.* **2015**, *71*, 3−8.
(65) Kuhelj, R.; Dolinar, M.; Pungercar, J.; Turk, V. The Preparation of Catalytically Active Human Cathepsin B from Its Precursor Expressed in Escherichia Coli in the Form of Inclusion Bodies. *Eur. J. Biochem.* **1995**, *229*, 533−539.
(66) Feng, B. Y.; Shoichet, B. K. A Detergent-Based Assay for the Detection of Promiscuous Inhibitors. *Nat. Protoc.* **2006**, *1*, 550−553.

DOI: 10.1021/acs.inorgchem.9b01882
Inorg. Chem. 2019, 58, 12334−12347